catalysts

MDPI

Article

Feed Effects on Water–Gas Shift Activity of M/Co_3O_4-ZrO_2 (M = Pt, Pd, and Ru) and Potassium Role in Methane Suppression

Satyapaul A. Singh [1,2,*], Yaddanapudi Varun [1], Priyanka Goyal [1], I. Sreedhar [1] and Giridhar Madras [3]

[1] Department of Chemical Engineering, Birla Institute of Technology and Science (BITS) Pilani, Hyderabad Campus, Jawahar Nagar, Kapra Mandal, Hyderabad 500078, India
[2] Materials Center for Sustainable Energy & Environment (MCSEE), Birla Institute of Technology and Science Pilani, Hyderabad Campus, Jawahar Nagar, Kapra Mandal, Hyderabad 500078, India
[3] Department of Chemical Engineering, Indian Institute of Technology, Hyderabad 502285, India
* Correspondence: satyapaul@hyderabad.bits-pilani.ac.in; Tel.: +91-40-66303-566

Abstract: Water–gas shift (WGS) is an industrial process to tackle CO abatement and H_2 upgradation. The syngas (CO and H_2 mixture) obtained from steam or dry reformers often has unreacted (from dry reforming) or undesired (from steam reforming) CO_2, which is subsequently sent to downstream WGS reactor for H_2 upgradation. Thus, industrial processes must deal with CO_2 and H_2 in the reformate feed. Achieving high CO_2 or H_2 selectivities become challenging due to possible CO and CO_2 methanation reactions, which further increases the separation costs to produce pure H_2. In this study, M/Co_3O_4-ZrO_2 (M = Ru, Pd and Pt) catalysts were prepared using sonochemical synthesis. The synthesized catalysts were tested for WGS activity under three feed conditions, namely, Feed A (CO and steam), Feed B (CO, H_2 and steam) and Feed C (CO, H_2, CO_2 and steam). All the catalysts gave zero methane selectivity under Feed A conditions, whereas the methane selectivity was significant under Feed B and C conditions. Among all catalysts, PtCZ was found to be the best performing catalyst in terms of CO conversion and CO_2 selectivity. However, it still suffered with low but significant methane selectivity. This best performing catalyst was further modified with an alkali component, potassium to suppress undesirable methane selectivity. All the catalysts were well characterized with BET, SEM, TEM to confirm the structural properties and effective doping of the noble metals. Additionally, the apparent activation energies were obtained to showcase the best catalyst.

Keywords: WGS; reformate feed; methane suppression; noble metal; Co_3O_4; ZrO_2; activation energy

Citation: Singh, S.A.; Varun, Y.; Goyal, P.; Sreedhar, I.; Madras, G. Feed Effects on Water–Gas Shift Activity of M/Co_3O_4-ZrO_2 (M = Pt, Pd, and Ru) and Potassium Role in Methane Suppression. *Catalysts* **2023**, *13*, 838. https://doi.org/10.3390/catal13050838

Academic Editors: Ridha Djellabi, Melissa Greta Galloni and Sebastiano Campisi

Received: 29 March 2023
Revised: 29 April 2023
Accepted: 2 May 2023
Published: 4 May 2023

1. Introduction

The development of efficient and zero emission vehicles is a major challenge for automobile industries. It is also challenging for process industries to generate high purity H_2 for proton exchange membrane fuel cells (PEMFC) to further address the clean energy requirements. H_2 production route map in the process industries have series of steps such as reforming, water–gas shift, preferential CO oxidation and pressure swing adsorption to capture CO_2. Among these steps, water–gas shift reaction is a route for hydrogen upgradation using the reformate feed obtained from reformers [1,2]. Using H_2 as feed, the PEMFCs can generate clean energy. However, PEMFCs demand high purity H_2 with extremely low CO impurities (less than 10 ppm) and other hydrocarbons to avoid the poisoning of Pt membrane. Thus, all the catalysts in the downstream processes after reforming must be designed to maximize the H_2 purity. Typically, the dry reformate gas mixture contains H_2, CO at high compositions, and the other components such as CO_2, unreacted hydrocarbons at low compositions [1]. The CO composition is minimized with water–gas shift (WGS) reaction by facilitating a reaction with superheated steam (often

in excess quantity). The typical WGS reaction for upgrading H_2 and minimizing CO is as follows,

$$CO + H_2O \rightleftarrows CO_2 + H_2 \cdot \Delta H_{298K} = -41 \text{ kJ mol}^{-1} \quad (1)$$

Industries implement two stages for converting CO into CO_2 from H_2 rich feed by conducting high temperature and low temperature water–gas shift (HTS and LTS). HTS operates in a temperature range of 350–500 °C to reduce CO composition below 4%, whereas LTS operates in the range of 150–300 °C to bring down the CO compositions below 0.2% [1,3]. These two stages (HTS and LTS) significantly improve the H_2 composition. After that, CO_2 will be removed using pressure swing adsorption to obtain pure H_2.

The industrial catalysts used for HTS and LTS are Fe-Cr oxides and Cu-ZnO-Al_2O_3 [1,4–7]. $Fe_2O_3/Cr_2O_3/CuO$ is used as commercial catalyst for high temperature water gas shift reaction in which Cr becomes carcinogenic as it is oxidized to Cr^{6+} from Cr^{3+} [8]. To overcome these problems, various metal oxide catalysts with noble metal impregnation or substitution were developed. In recent years, a significant use of reducible supports (such as ceria) in conjunction with noble metals for LTS was observed [9]. With the usage of reducible oxides, the interplay of lattice oxygen vacancies and active metal sites in the reaction mechanism is significant. Oxygen vacancies play a crucial role in the adsorption of water and/or CO molecule, active metal sites can enhance the activation of the molecules leading to the formation of intermediates such as carboxyl and formates [10]. CeO_2 is one of such metal oxides that can function as oxygen buffer under exhaust conditions by releasing/acquiring oxygen through redox processes involving the Ce^{4+}/Ce^{3+} couple [11]. Senanayake et al. [12] also tested ceria alone as a catalyst and showed that reduced Ce^{3+} and oxygen vacancies contribute to the production of hydrogen through the reaction. Other than CeO_2, low temperature water–gas shift is a well explored reaction on various reducible and non-reducible catalysts such as TiO_2, ZrO_2 and Al_2O_3 [13–15]. The effect of noble metals and transition metals on reducible oxides such as ceria were widely studied [16–19]. Pt- and Au-based catalysts on other reducible catalysts showed high catalytic activity for LTS, whereas Ni- and Fe-based catalysts were reported for HTS [6,20–23]. The water–gas shift activity of a support majorly depends on the reducible nature of the catalysts, strong metal support interaction (SMSI), oxygen storage capacity (OSC) and surface nature of the support [24–27]. By acquiring the mentioned properties, the high catalytic activity and stability can be achieved.

Mierczynski et al. [28] studied the activity of monometallic (Pd, Ru, Ni and Cu) catalysts supported on $ZnAl_2O_4$ spinel support. While Ru catalysts showed the highest conversion at high temperature, the Cu catalysts were shown to be good at low temperatures. Pd catalysts showed poor performance due to intermetallic PdZn compounds at intermediate temperatures due to interaction between the metal and the support. The lowest activity was observed for Ni catalysts because only a small amount of nickel species dispersed on the support surface. The terminal OH groups bound to active metal of the $ZnAl_2O_4$ spinel reacted with carbon monoxide and formed formate bridges and obtained H_2 and CO_2 as the products. Hu et al. [29] modified the Pd-based catalysts with Zn and showed that addition of Zn weakened the electron-accepting ability of the catalyst and increased the electron-donating ability and promoted the LTS activity. The reaction pathway is an associative mechanism through COOH intermediate, which is same as the Pd catalyst.

The effect of the noble metal Pt on ceria support was also shown by Jacobs et al. [30]. In this study, Pt facilitated partial reduction in ceria and promoted formate decomposition through enhanced C-H bond rupture rate, and ceria helped bridging the OH groups such that formates could be formed upon CO adsorption. Mandapaka et al. [10] studied the WGS over Pt supported on ceria. An associative carboxyl mechanism was proposed. The rate limiting step was considered as the dissociation of surface carboxyl species over Pt to give surface bound CO_2 and H. DFT studies for ceria catalyst suggested the reaction mechanism steps as reversible adsorption of CO on ionic platinum site and of H_2O on the surface vacancy on ceria. The adsorbed H_2O then disintegrates to give OH surface species, which then react with adsorbed CO species to form surface COOH and H [27].

The COOH surface species then disintegrate to form CO_2 and H. The products then desorb and complete the catalytic cycle with 90% conversion at 250 °C. It was also shown that the use of noble metal catalysts supported on zinc and platinum co-doped ceria can convert the WGS into a single-stage process. Both metal and support were found to be equally effective in the reaction mechanism in which CO adsorbs on the Pt site while H_2O is adsorbed and activated on the ceria site. Shinde et al. [31] studied Pd-modified Ni/CeO_2 to prevent CO methanation while improving H_2O dissociation. Vignatti et al. [32] showed that $Pt/Ce_xZr_{1-x}O_2$ catalysts with $x \geq 0.5$ were more active than Pt/CeO_2 or Pt/ZrO_2 as Zr tends to increase the surface area as well as the reducibility of ceria, while also increasing the concentration of surface OH groups that are formed on Ce^{3+} reduced sites. These terminal OH groups participate in the WGS reaction resulting in an associative mechanism via formate formation. Ding et al. [33] provided comparative results for Pt single atoms and Pt nanoparticles as Pt is believed to be an exceptionally active catalyst for the WGS. It was observed that only Pt nanoparticles showed activity for LTS while the Pt single atoms on HZSM-5 behaved as spectators due to the strong binding of the CO molecules. This shows the poisonous effect of CO on Pt atoms. Improvement in performance and CO conversion was observed with the lattice substitution. Studies conducted by Petallidou et al. [34] showed the catalytic activity showed better catalytic performance with lattice substituted Pt than the impregnation. The performance trend was observed as $Pt/Ce_{0.9}Ti_{0.2}O_{2-x} > Pt/CeO_2 > Pt/TiO_2$.

The variety reducible supports with noble and transition metals as catalysts may satisfy the requirements for PEMFCs in eliminating entire CO in the gas mixture under the feed conditions of CO and steam. However, under real conditions, the reformate gas mixture (from the steam or dry reforming unit) contains CO along with other components such as CO_2, H_2 as shown in Scheme 1. This often results in CH_4 formation as a side product, that too in prominent compositions. The WGS catalysts under reformate feed conditions can result side reactions such as CO and CO_2 methanation which decreases the H_2 yield and CO conversion. Thus, the study of catalytic-inhibiting effects of CO_2 and H_2 in the feed is an interesting aspect for practical applications of WGS.

Providing strong metal support interaction (SMSI) and oxygen storage capacity (OSC) are merely not sufficient to reduce the methanation. Thus, alkali modifications were investigated to suppress the methanation affinity. The addition of alkalis (electron donors) create electron cloud surrounding surface and increases the chemisorption of electron acceptor species such as CO and O_2 and suppresses the chemisorption of electron donor species such as H_2 and olefins [35]. Maneerung et al. [35] showed that $LaNiO_3$ perovskite materials were not equally effective for HTS under reformate feed conditions. These catalysts were favorable for methane selectivity through CO_2 methanation. However, methanation was successfully prevented by the addition of K on the perovskite surface with an optimum of 5 wt% K over La_2O_3. K occupies the interface between La_2O_3 and Ni nanoparticles. K, La_2O_3 and Ni act as adsorbents for water, CO_2 and H_2, respectively. K aids in providing hydroxyl groups to combine with the CO and form HCOO intermediates. The doped catalyst was found to stable for an operating period of 5 h and resulted in 90% CO conversion at 350 °C. Ang et al. [22] attributed the methanation suppression using 5 wt% K doping on ceria supported nickel ($Ni/5K/CeO_2$) to the inhibition of the formation of nickel sub-carbonyls. These are precursors for methanation reaction and are prevented due to the interaction between Ni and K. Additionally, as K is hygroscopic, K was found to enhance a reduction in CeO_2 and promote water dissociation on reduced CeO_2 to form hydroxyl (OH) groups, which dissociate further into adsorbed oxygen that reacts with adsorbed CO on Ni to form adsorbed carbon dioxide CO_2. $Ni/5K/CeO_2$ was found to be stable for 100 h of time-on-stream condition.

Noble metals such as Pt and Pd were proved to be effective catalysts for the WGS. Watanabe et al. [36] evaluated the activities of $Pd/alkali/Fe_2O_3$ catalysts with different ratios of alkali/Pd (alkali: Li, Na, K or Cs). The optimum K/Pd molar ratio was found to be 2, and the reaction proceeded through the redox mechanism using the lattice oxygen,

which was regenerated by H_2O, while reducing the Fe_2O_3 to Fe_3O_4. Order of reducibility of these catalysts was K-impregnated > Cs-impregnated > Na-impregnated > Pd/Fe_2O_3 ≈ Li-impregnated alkali metals such as Na (51.2% conversion), K (83.1% conversion) and Cs (72.2% conversion) drastically enhanced WGS activity, except for Li-loaded (only 11.5% conversion) catalyst. The role of alkalis such as K and Na was studied on various reducible supports [22,29,30].

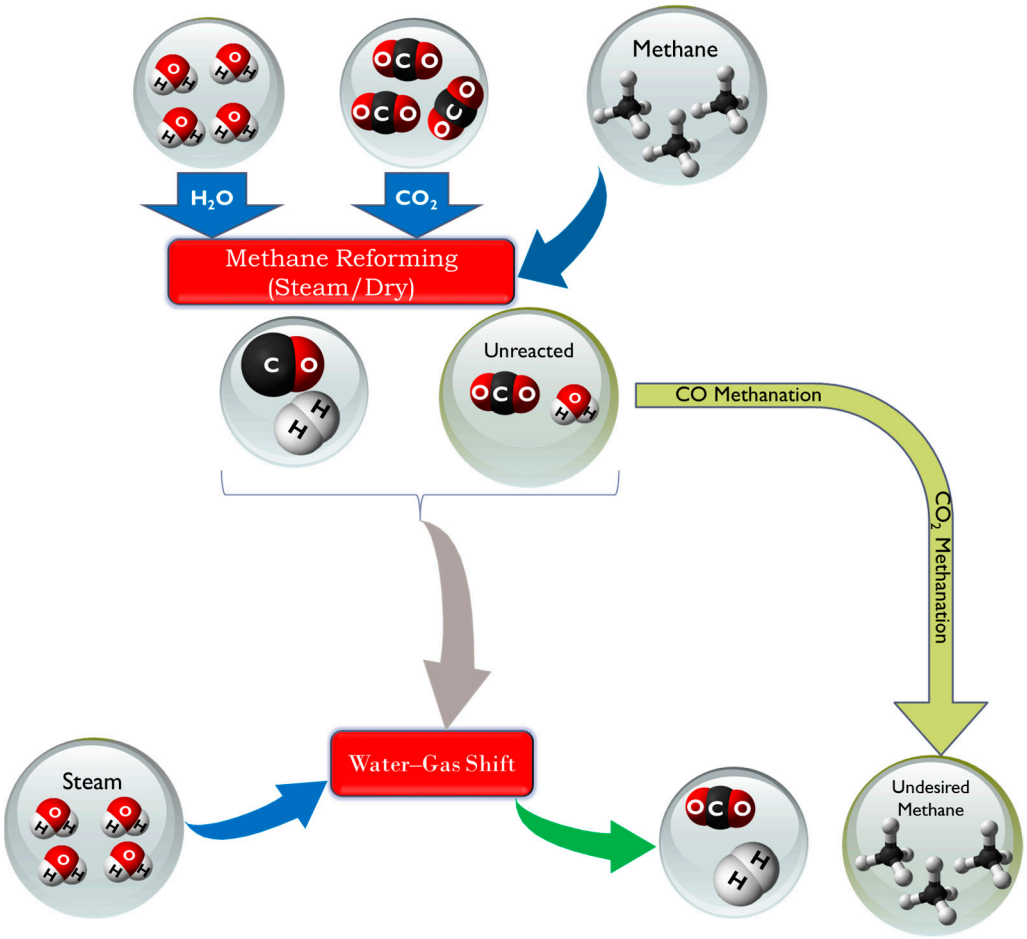

Scheme 1. Effect of reformate feed mixture of CO, CO_2 and H_2 on water–gas shift activity.

This study focuses on the development of thermally stable composite supports using sonochemical synthesis and the effect of noble metals on WGS activity. A mixed metal composite support containing reducible Co_3O_4 and non-reducible ZrO_2 was prepared and the role of noble metals (Pt, Pd and Ru) was investigated for WGS. The catalytic activity of the M/Co_3O_4-ZrO_2 (M = Pt, Pd and Ru) was studied with three different dry feed gas mixtures, to investigate the role of H_2 and CO_2 in the feed on WGS activity. The suppression of methanation ability under realistic reformate gas feed condition using K as promoter was also investigated. All the catalysts were characterized with XRD, XPS, TEM, BET and TPR studies.

2. Results and Discussion

2.1. X-ray Diffraction and BET Measurements

XRD patterns of the synthesized catalysts are shown in Figure 1, which confirmed the presence of both Co_3O_4 and ZrO_2 phases by comparing with JCPDS database files 00–042–1467 and 00–003–0640, respectively. The CZ composite consisted of cubic Co_3O_4 (a = b = c = 8.084 Å, space group: Fd-3 m) and cubic ZrO_2 (a = b = c = 5.103 Å, space group: Fm-3 m) phases [37,38]. Monoclinic ZrO_2 and cubic CoO phases were possible

in the synthesis of composites, but these phases were not detected in the synthesized materials. The most possible prominent peaks associated with metals Pt (111), Pd (111) and Ru (101) at 39.67°, 40.42° and 44.37° were not found from the XRD of PtCZ, PdCZ and RuCZ. As the doping % was limited to 2%, the detection was not possible from XRD. However, a slight shift in 2θ values was observed because of the different ionic radius of metals and variation in lattice parameters [37,38]. This further indicates the possibility of ionic catalysts, where dopant replaces Co or Zr and bonds with lattice oxygen upon the nucleation and growth. In KPtCZ, the presence of K was not detectable, but a very small peak at 39.7° corresponding to Pt (111)/PtO_2 (101) was noticed. In the synthesis of KPtCZ, the K impregnation was implemented using reducing agents. Due to the reducing agents, weakly bound Pt ion in the lattice may diffuse to surface and form PtO_2 cluster and it was possible during K impregnation on PtCZ. Upon investigating XPS analysis, no metallic Pt was found in KPtCZ and these results were explained in Section 2.4.

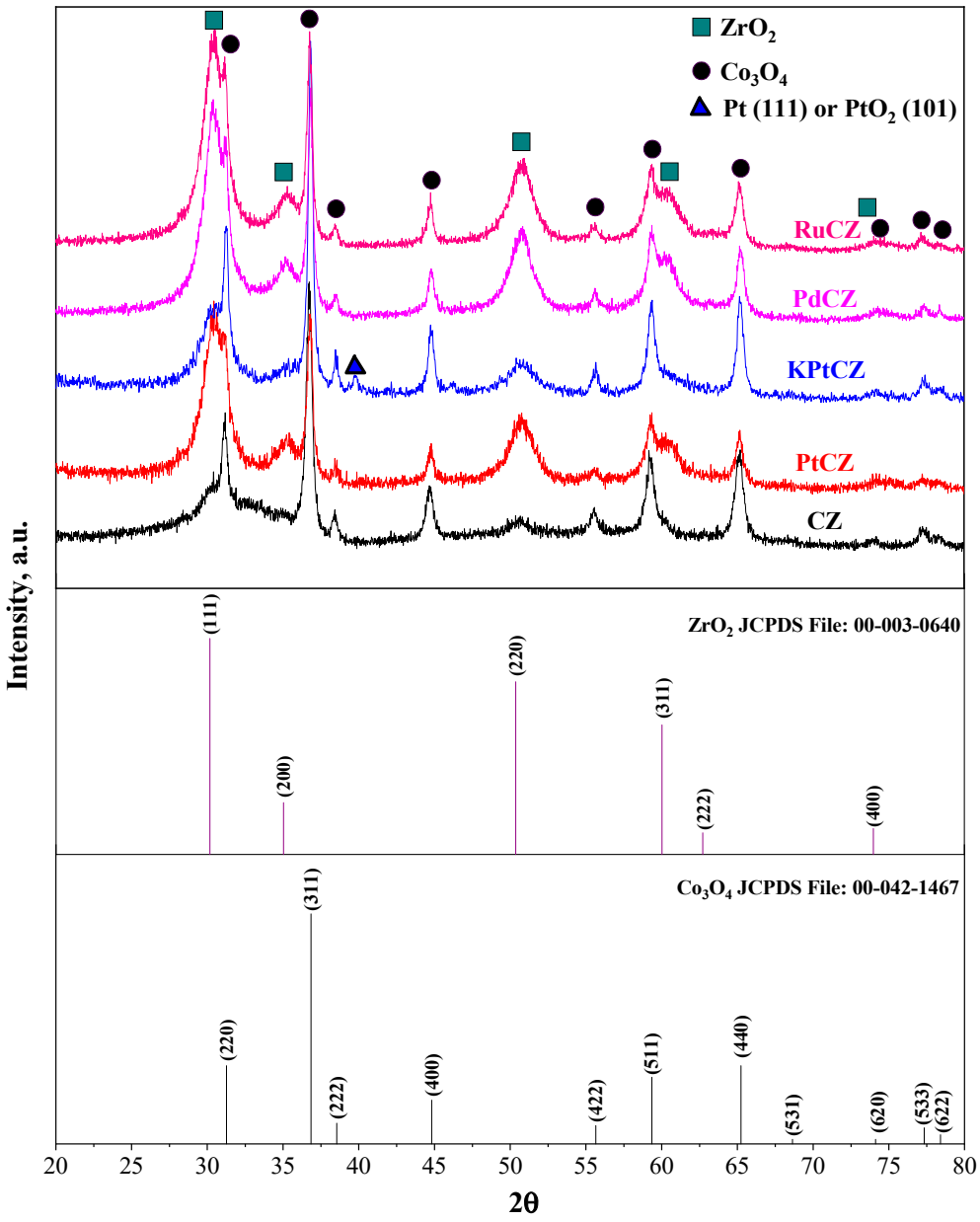

Figure 1. XRD pattern for CZ composite catalysts.

The adsorption–desorption isotherms for all the materials indicated Type II isotherms (as shown in Figure 2) and offered unrestricted monolayer–multilayer adsorption. Type H3 hysteresis was noticeable for the synthesized catalysts, indicating the possibility of meso- and micro-porous materials. The specific surface areas, pore volumes, mean pore diameters and crystallite sizes (using Debye–Scherrer relation) of CZ, PtCZ, KPtCZ, PdCZ and RuCZ are listed in Table 1. In general, the sharper XRD peaks indicate larger crystallite sizes, whereas the broader peaks correspond to smaller crystallite sizes. The most intense peak of ZrO_2 (111) at 30.1° was merged with Co_3O_4 (220) at 31.2°. Thus, the most intense sharper peak corresponds to Co_3O_4 (311) at 36.8° and was considered for crystallite size using the Debye–Scherrer equation. Interestingly, the crystallite size of KPtCZ was found to be high compared to all the materials. On the contrary, its surface area and pore volumes were also found to be higher. This could be due to the additional chemical reduction step associated with K impregnation. The chemical reduction was able to create more pores and effective K dispersion, which led to achieve enhanced surface area and pore volumes (from Figure 2e and Table 1).

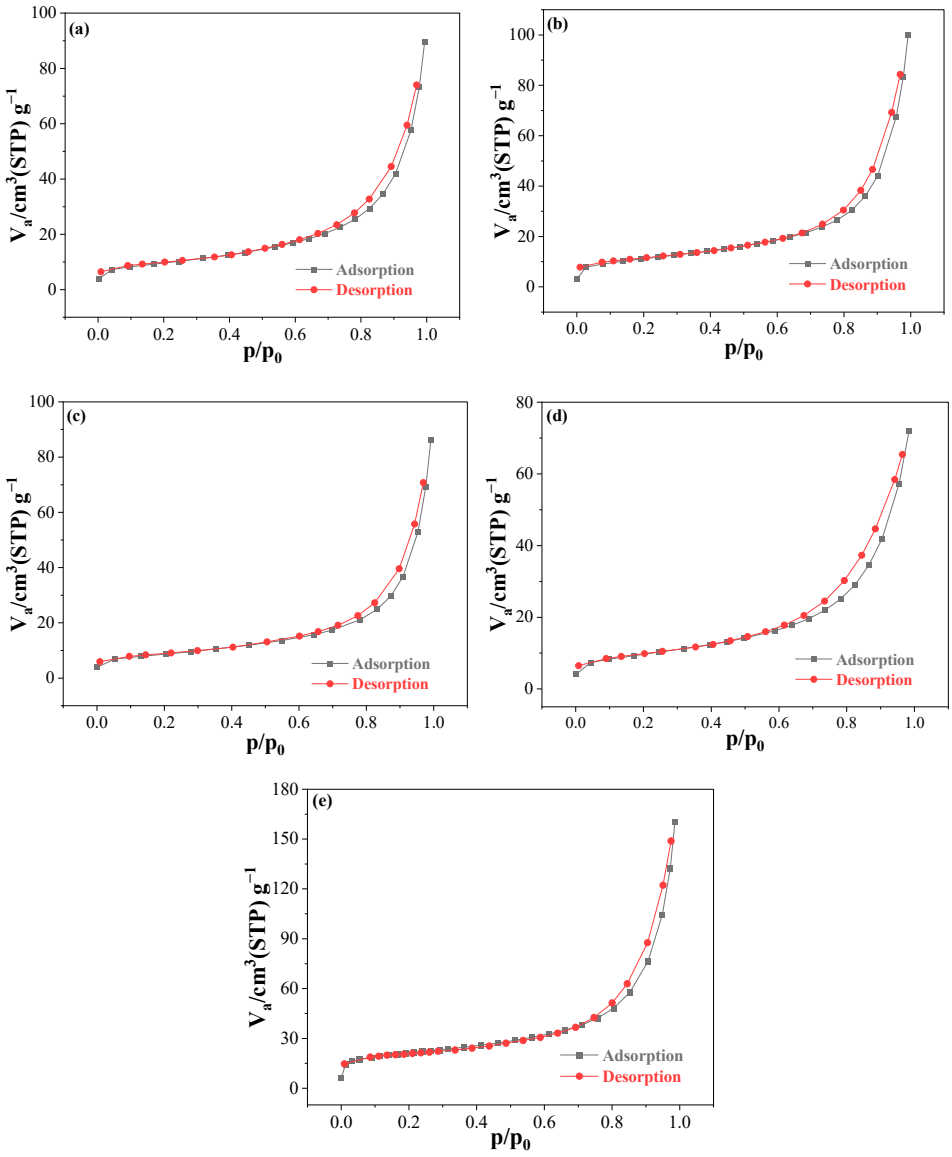

Figure 2. Adsorption–Desorption curves for (**a**) CZ (**b**) RuCZ (**c**) PdCZ (**d**) PtCZ (**e**) KPtCZ.

Table 1. Characteristics of CZ, PtCZ, KPtCZ, PdCZ and RuCZ from BET and XRD analysis.

Catalyst	Surface Area, m^2/g	Total Pore Volume, cm^3/g	Mean Pore Diameter, nm	Crystallite Size, nm
CZ	34	0.133	15.5	18.1
RuCZ	40	0.150	15.1	20.4
PdCZ	31	0.130	16.9	21.5
PtCZ	33	0.116	13.4	19.8
KPtCZ	74	0.248	13.5	24.2

2.2. Scanning Electron Microscopy and Transmission Electron Microscopy Studies

The scanning electron microscope (SEM) images shown in Figure 3 indicates the fine and homogenous particles formation with less porosity. The pore volume of KPtCZ was improved, as shown in Table 1. The elemental analysis using energy dispersive X–ray diffraction (EDX) analysis of the RuCZ, PdCZ, PtCZ and KPtCZ on Figure 4 confirmed the presence of dopants of Ru, Pd, Pt and K.

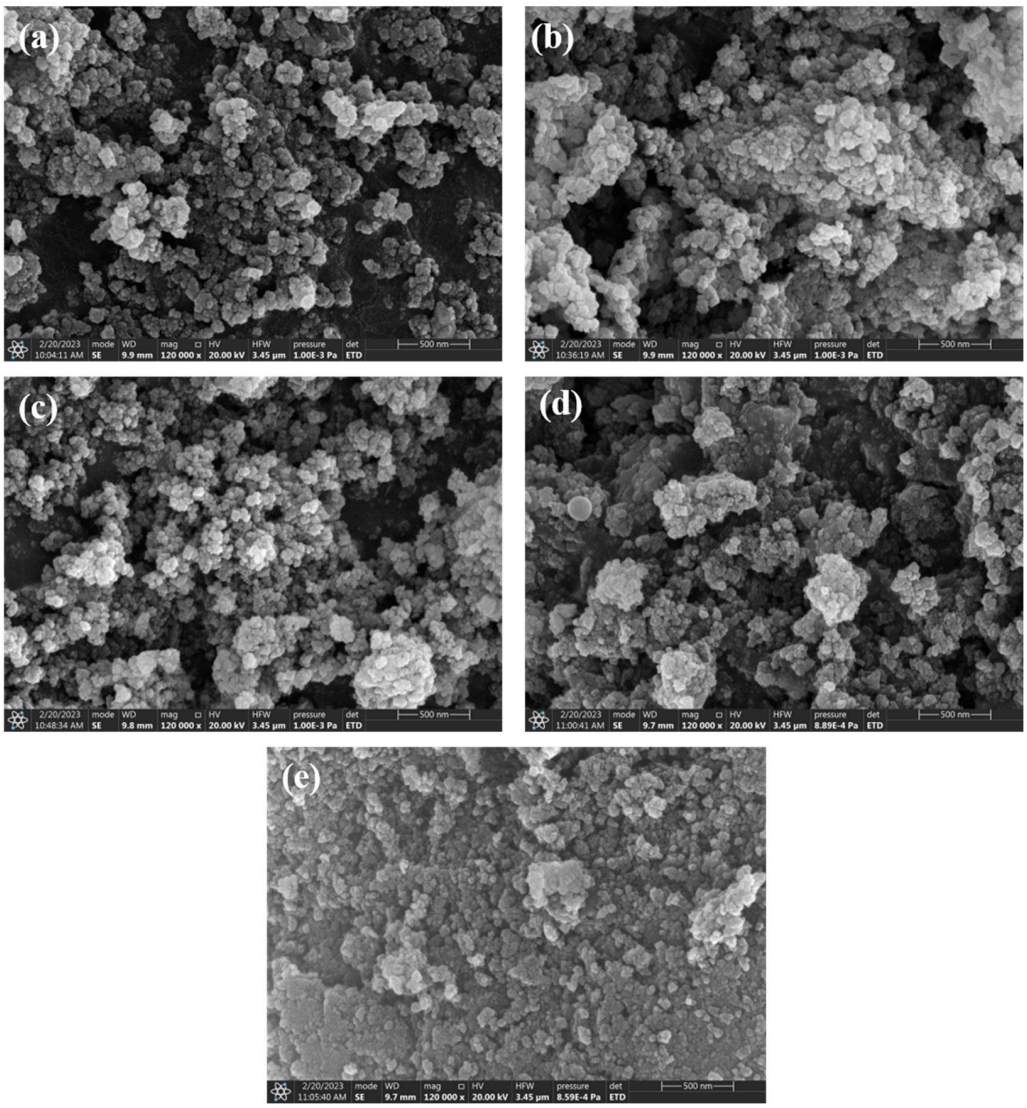

Figure 3. Scanning electron microscope images of (**a**) CZ (**b**) RuCZ (**c**) PdCZ (**d**) PtCZ and (**e**) KPtCZ.

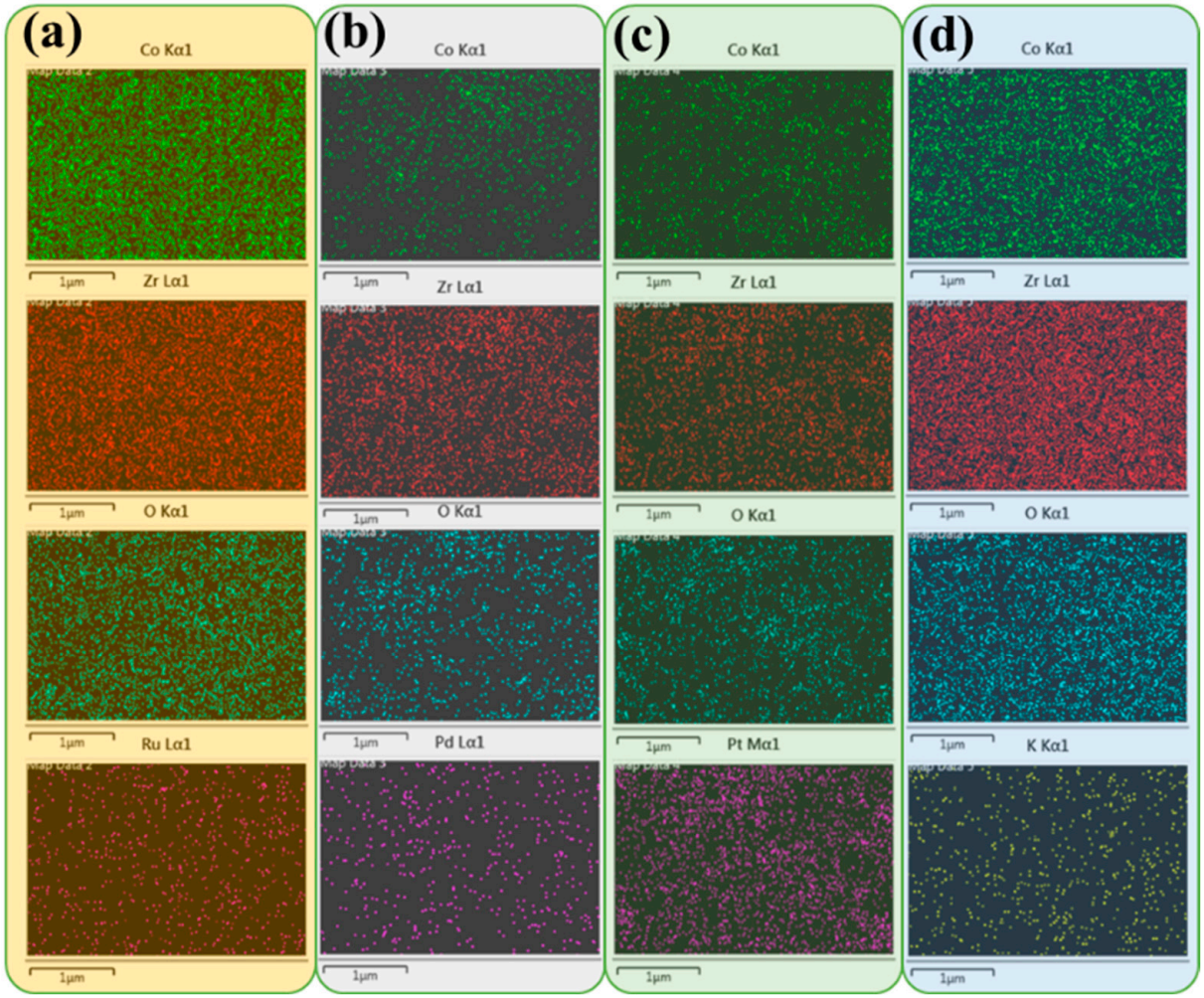

Figure 4. EDX mapping of (**a**) RuCZ (**b**) PdCZ (**c**) PtCZ and (**d**) KPtCZ.

From Figure 5, ZrO_2 and Co_3O_4 phases were confirmed with HRTEM results by analyzing fringes of the d–spacing of the particles. The large particles indicate the ZrO_2 phase whereas smaller particles were confirmed as Co_3O_4. The presence of Pt (111), Pd (111) and Ru (110) was found in the lattice fringes of the particles. The (111), (222), (220) planes of ZrO_2 and (311), (422) planes of Co_3O_4 were confirmed by analyzing diffraction rings (Figure 5a–f). Figure 5e,h showed very small clusters of Pt, Pd and Ru dispersed in a solid solution. The cluster embedded in the support were around 2–3 nm, as shown in Figure 5e,h,k,n. These clusters shared complete boundary with the support material due to the substitution. This is an advantageous feature to enhance the metal support interaction and keep the noble metal isolated at elevated temperatures by avoiding thermal sintering. The resistance towards sintering and effective dispersion lead to high catalytic activity. The ionic substitution of Pt and Pd was due to the atomically dispersed Pt, Pd and Ru in the support, which can oxidize by utilizing bulk oxygen or oxygen vacancies in the support [39,40]. As the active metals were substituted in the support material, slight deviations in the interplanar spacing values were possible compared to noble metal reference data. Figure 5e,k,n shows the HRTEM images of PtCZ, KPtCZ, PdCZ and RuCZ and the d–spacing of lattice fringes for Pt, PD and Ru were observed as 2.25 Å, 1.94 Å and 2.04 Å, respectively. This d–spacing values were closely matched with the reference Pt (111), Pd (200) and Ru (100) planes.

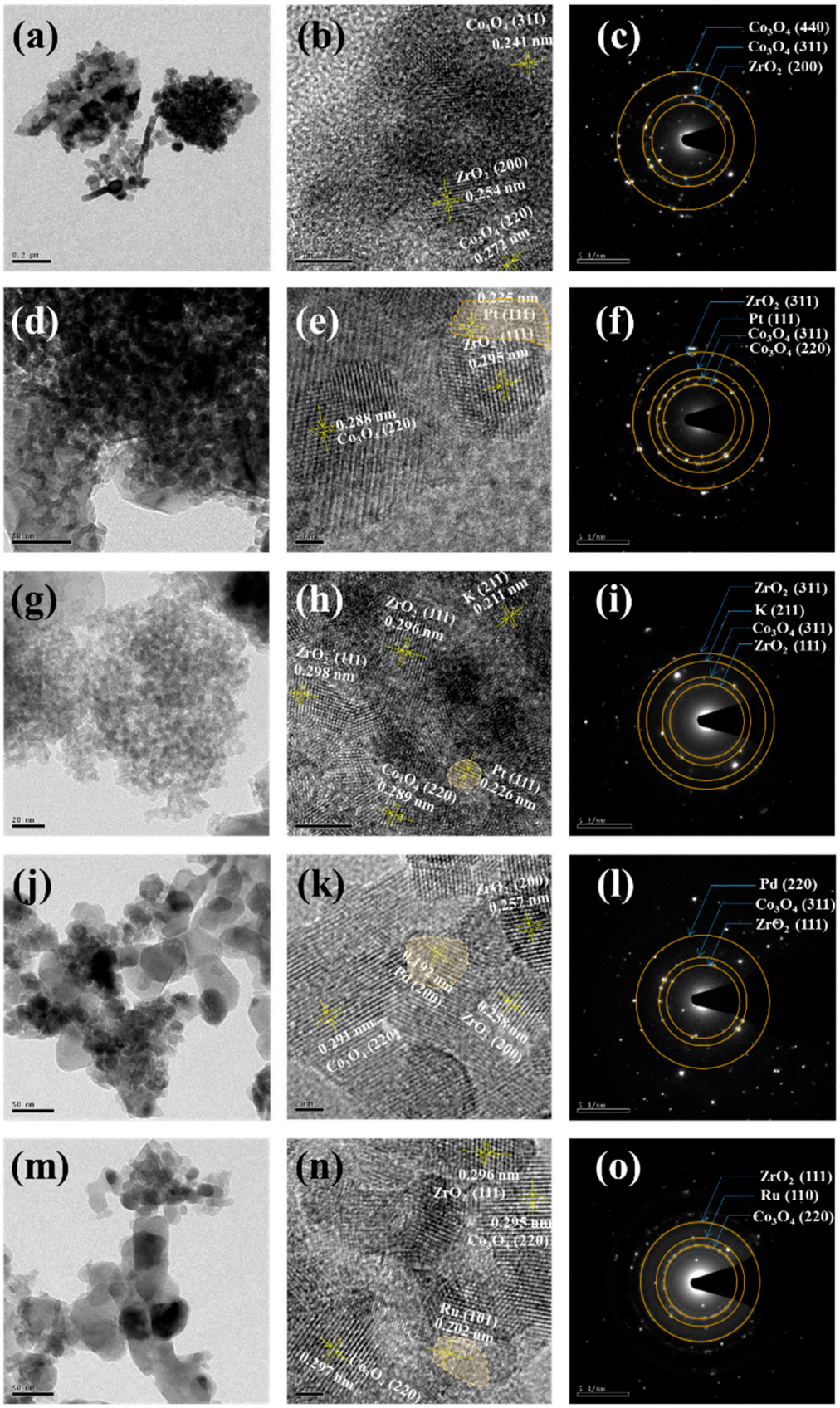

Figure 5. Bright field, high resolution and selective area diffraction images of (**a**–**c**) CZ, (**d**–**f**) PtCZ, (**g**–**i**) KPtCZ, (**j**–**l**) PdCZ, (**m**–**o**) RuCZ.

2.3. Catalytic Activity Studies

The synthesized catalysts were subjected to catalytic activity studies under different feed conditions. To understand the behavior of feed on the surface of CZ composite catalysts, different feed compositions were maintained. The total flow rate of 100 mL/min (at NTP) dry gas flow mixed with superheated steam at 150 °C and introduced to the reactor. Dry gas concentrations of CO: N_2 = 2%: 98% (Feed A), CO: H_2: N_2 = 2%: 35%: 63% (Feed B) and CO: H_2: CO_2: N_2 = 2%: 35%: 14%: 49% (Feed C) were maintained in the catalytic activity studies. The equilibrium analysis was performed by minimizing the Gibbs free energy under different feed conditions. The Peng–Robinson equation of state was implemented to assess the real behavior of the gases. From this analysis, both conversions and selectivities were benchmarked at all operating temperatures under different feeds. Further, two sets of reactions were implemented. In one set, only WGS reaction was implemented, whereas in another set, both CO and CO_2 methanation were considered along with WGS.

From the results shown in Figure 6a, it is evident that the role of side reactions was insignificant for Feed A. The equilibrium conversion at 300 °C was 99.92% and 99.94% with and without side reactions. Though the CO conversions were similar, a significant change in methane selectivity was noticed due to side reactions. At 300 °C, the methane selectivity was found to be 7.3% with side reactions (shown in Figure 6b), whereas no methane selectivity was possible in absence of side reactions. Thus, 100% methane selectivities were obtained for Feed A conditions. Under Feed B (H_2 rich stream) and Feed C (H_2 and CO_2 rich stream), the higher conversions of CO are possible due to side reactions. From Figure 6c,e, the CO conversions were found to be 98.7% and 89.3% at 300 °C for Feed B and C in absence of side reactions. Due to CO and CO_2 methanation, the equilibrium CO conversions were increased to 100% and 99.48% for Feed B and C at 300 °C. High methanation trend was clearly evident from Figure 6d,f as well. For Feed B, the CH_4 selectivities can go up to 100% due to side reactions at temperatures below 325 °C, whereas the CH_4 selectivity was found to be 49.4% at 300 °C and it decreased with temperature under Feed C. The equilibrium conversions and selectivities were compared with the experimental data in Table 2 for benchmarking.

Figure 7a shows the catalytic activity of CZ composite under different feed conditions. CZ composites started showing activity from 220 °C and the conversions increased with temperature. At 300 °C, CZ composites showed CO conversion of 16%, 11% and 8% under different feed conditions (Feed A, B and C). The presence of hydrogen in the feed inhibited the catalytic activity due to its reduction ability. Additionally, the presence of both H_2 and CO_2 in feed further decreases the catalytic activity due to blockage of active sites and allow CO to compete for the adsorption sites [41]. In all three feed conditions, no methanation was observed below 320 °C (from Figure 7b). These experiments provided information about the role of support (CZ composite) for WGS activity within the range of 180–320 °C. The effect of reformate feed condition on RuCZ and PdCZ catalysts is shown in Figure 7c–f. The CO conversions greater than 95% were observed at 320 °C in both Feed A and Feed B conditions for RuCZ, whereas under Feed C condition of CO_2 and H_2 rich feed, the CO conversions increased to a maximum of 84% at 300 °C and continued to decrease as the temperature rose. Interestingly, the methane selectivity was found to be very high prominent under both Feed B and C conditions. For instance, at 320 °C, the methane selectivity was found to be 38% and 47%, respectively, under both Feed B and Feed C conditions. Under Feed C condition, the methane selectivity was continued to increase up to 77% at 400 °C, indicating the methanation ability of the Ru active sites in a catalyst. This could be due to CO_2 methanation resulted from CO_2 rich feed. It indicates that Ru-based catalysts are not potential candidates for suppressing methanation in water–gas shift reaction under reformate feed and our results are in line with Utaka et al. [42] At 320 °C, PdCZ was able to achieve 47%, 73% and 56% of CO conversions for Feed A, B and C, as seen in Figure 7e. These conversions were significantly lower than RuCZ catalyst. Especially under Feed B condition, the CO conversions were high compared to other feed

conditions. This was due to high affinity of Pd in dissociating H_2 to atomic hydrogen [37]. However, the atomic hydrogen was more prone to form methane, the methane selectivities were found to be significantly higher in 220–440 °C. The maximum conversions of 96% at 400 °C and 94% at 360 °C were observed on PdCZ catalysts under Feed A and Feed B conditions. The methanation was negligible under Feed A condition but it is significant in other cases. Methane formation was even observed at low temperatures of 220 °C under both Feed A and B conditions. From these studies, PdCZ was not an active catalyst for WGS under both reformate and pure feed conditions. Additionally, it was found to have poor methane suppression ability.

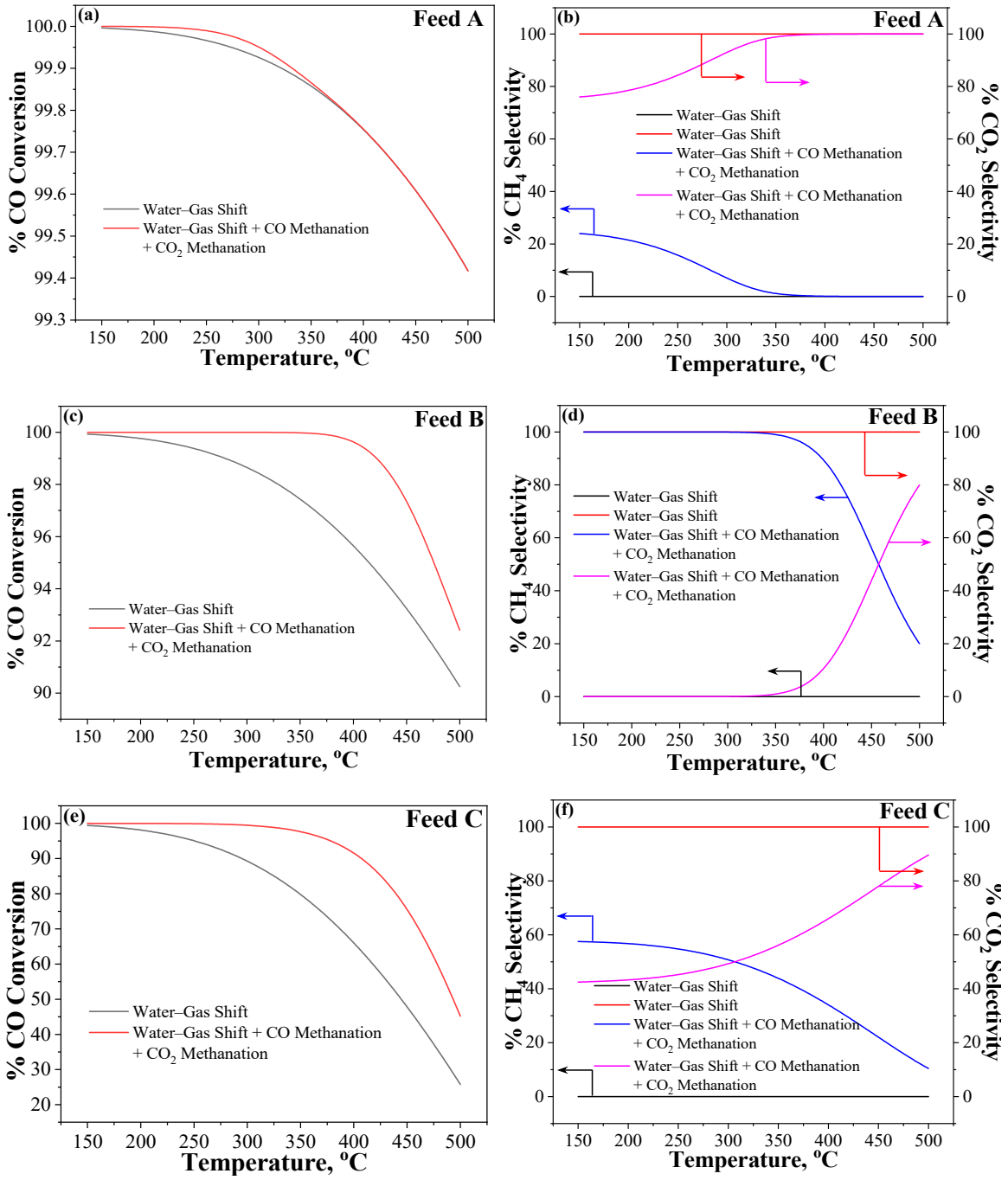

Figure 6. Equilibrium conversion and selectivities for WGS under reformate feed conditions.

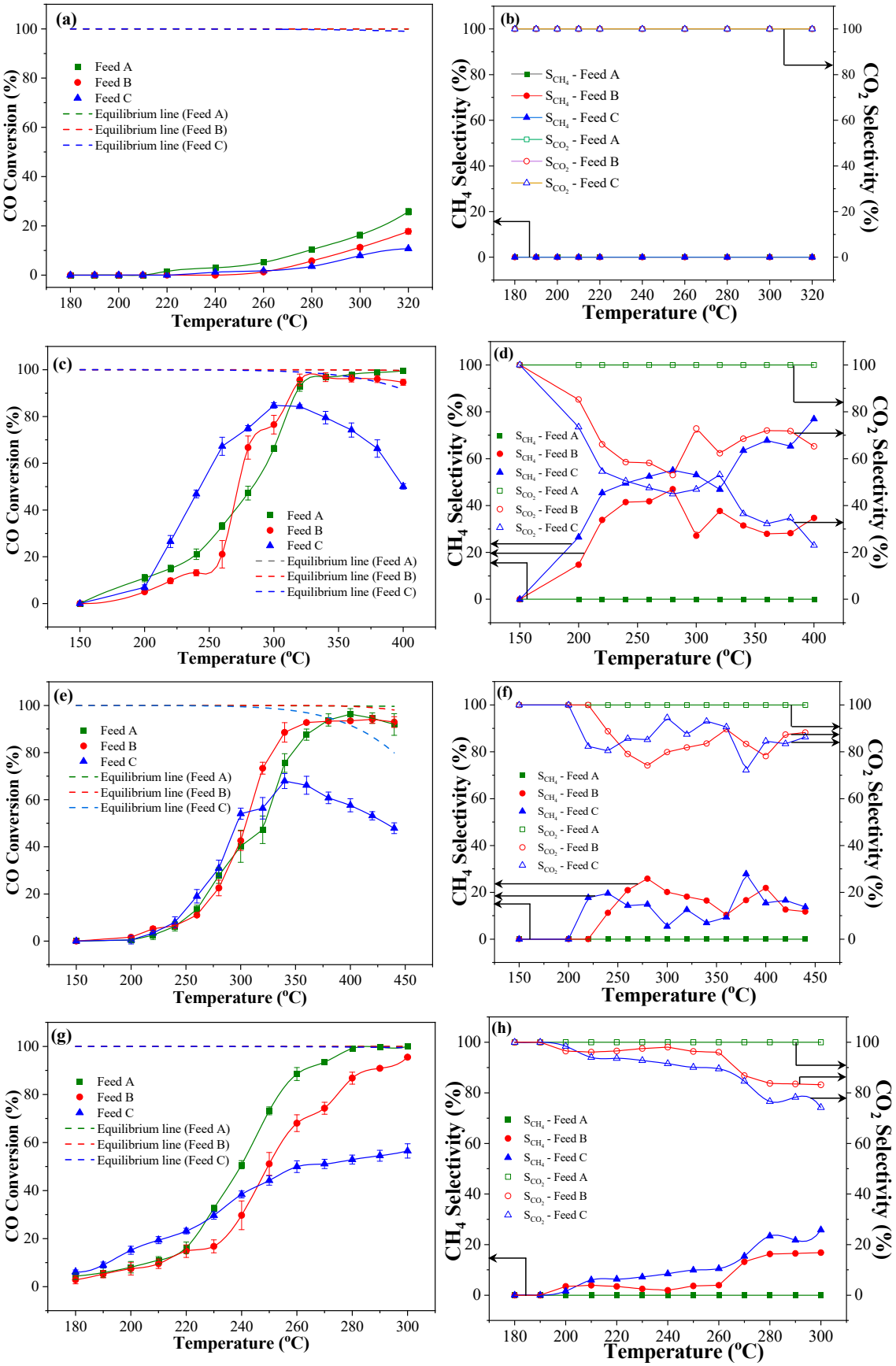

Figure 7. *Cont.*

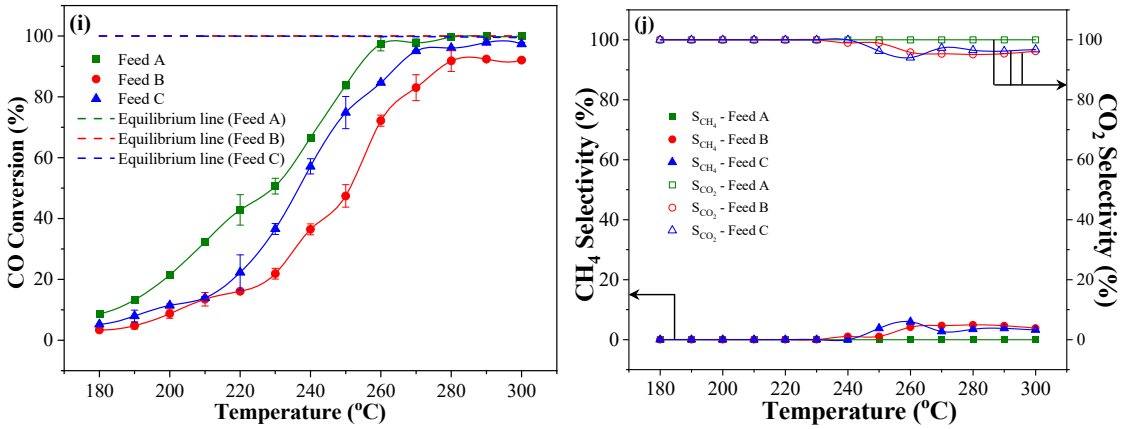

Figure 7. Conversion of CO, methane and CO_2 selectivities with temperature under different feed conditions with (**a**,**b**) CZ, (**c**,**d**) RuCZ, (**e**,**f**) PdCZ, (**g**,**h**) PtCZ and (**i**,**j**) KPtCZ catalysts. Dashed line indicates the equilibrium conversion considering WGS, CO and CO_2 methanation reactions. (Reaction Conditions: 150 mg loading, 1 cm bed length, Dry gas flowrate at NTP: 100 mL min^{-1}, 1 atm, Water flowrate at NTP: 0.05 mL min^{-1}, Steady state operation for 30 min at each temperature, dry gas composition (in vol%)–CO: N_2 = 2:98 (Feed A), CO: H_2: N_2 = 2:35:63 (Feed B) and CO: H_2: CO_2: N_2 = 2:35:14:49 (Feed C)).

Figure 7g shows the role of Pt for WGS activity under all feed conditions. With PtCZ catalysts, the WGS activity was observed even at 180 °C, unlike CZ composite catalysts that showed minimum activity at 220 °C. A 99% CO conversion was observed at 280 °C under Feed A condition. However, the CO conversion of 95% and 56% were observed at 300 °C under Feed B and C conditions. These conversions were exceptionally higher than PdCZ under all feed conditions, even higher than RuCZ catalyst except for Feed C condition. The presence of H_2 and CO_2 in feed inhibited the catalytic activity and allowed unfavorable side reactions such as methanation to occur. A maximum of 26% of methane selectivity was observed at 300 °C, whereas it was limited to 16% under Feed B condition. Like palladium, Pt is also an excellent catalyst for H_2 dissociation into atomic hydrogen [37]. Thus, the selectivity towards methane was significant, but it was found to be lower compared to PdCZ as well as RuCZ. For the application of PEMFC, the H_2 purity must be high with permissible concentrations of both CO and CH_4 [43]. Thus, minimizing methanation is essential in the WGS step. The catalysts offering methanation activity were not suitable for WGS to target PEMFC application. As PtCZ was found to be the best candidate among RuCZ and PdCZ in achieving high CO conversions and low methane selectivities, a further surface modification on catalyst was performed on PtCZ using K impregnation.

The impregnation of K on PtCZ catalyst suppressed methanation and allowed high CO conversions under all feed conditions, as shown in Figure 7i. ~100% CO conversion and rate of 9.09 µmol g^{-1} s^{-1} was observed at 300 °C under Feed A condition, whereas 98% and 93% (8.9 and 8.45 µmol g^{-1} s^{-1}) were observed under both Feed B and C conditions. The structural features of high surface area and pore volume also complimented its high catalytic activity. The catalytic activity in the presence of H_2 and CO_2 was found to be higher than the feed condition B in the presence of H_2 in feed. Interestingly, methanation was found to be negligible and methane selectivity of <4% was observed with KPtCZ catalyst under Feed B and C conditions and, like all other catalysts, no methane selectivity was observed under Feed A. A similar behavior was even observed in the case of WGS under H_2 rich feed as well as realistic reformate feed conditions, thus promoting the undesired methanation by utilizing H_2 activation. Promoting PtCZ catalyst with K offers electron density on catalysts surface, such a way that to increase the chemisorption affinity towards electron acceptor species such as CO and O_2 [44]. The alkali promoter further suppresses the chemisorption affinity of electron donor species such as H_2 [45]. The catalyst performance in comparison with literature and equilibrium data is shown in Table 2. KPtCZ

alone was close to the equilibrium CO conversion and minimum CH_4 selectivity at 300 °C, this indicates KPtCZ as the best candidate for WGS even under reformate feed conditions. All the experimental methane selectivities were found to be well below the maximum selectivity obtained from equilibrium studies.

Table 2. Literature comparison for water–gas shift studies.

Catalyst	Feed Details	Method of Synthesis	Temperature, °C	GHSV, h^{-1}	% Conversion of CO and % CH_4, CO_2 Selectivity	Reaction Rate, $\mu mol\ g^{-1}\ s^{-1}$	Ref.
$Mn_{2.94}Pt_{0.06}O_{4-\delta}$	CO:N_2 = 2:98 vol % Flowrate at NTP: 100 mL/min Water flowrate at NTP = 0.1 mL/min 100 mg catalyst	Sonochemical	250	48,000 (dry basis)	X_{CO} = 100% S_{CH4} = 0 S_{CO2} = 100%	12.24	[46]
$Ti_{0.84}Pt_{0.01}Fe_{0.15}O_{4-\delta}$	CO:N_2 = 2:98 vol % Flowrate at NTP: 100 mL/min Water vapor flowrate at 150 °C = 55 mL/min 300 mg catalyst	Sonochemical	280	48,000 (dry basis)	X_{CO} = 56% S_{CH4} = 0 S_{CO2} = 100%	2.59	[47]
1% Pt/Ceria	CO:H_2O:H_2:N_2 = 1.5:50:40:8.5 vol % 300 mg catalyst	Incipient wet impregnation	325	-	X_{CO} = 56% S_{CH4} = - S_{CO2} = -	-	[48]
$Pd/Ce_{0.83}Zr_{0.15}O_2$	CO:CO_2:H_2:N_2 = 2:10:40:48 vol% Flowrate at NTP: 100 mL/min Water flowrate at NTP = 0.1 mL/min 500 mg catalyst	Solution combustion	250	95,000 (dry basis)	X_{CO} = 94% S_{CH4} = - S_{CO2} = -	-	[49]
$Ce_{0.93}Zn_{0.05}Pt_{0.02}O_{2-\delta}$	CO:N_2 = 2:98 vol% Flowrate at NTP: 100 mL/min Water flowrate at NTP = 0.05 mL/min 200 mg catalyst	Sol-gel	300	48,000 (dry basis)	X_{CO} = 94% S_{CH4} = - S_{CO2} = -	8.33	[27]
RuCZ (Feed A)	CO:N_2 = 2:98 vol% Flowrate at NTP: 100 mL/min Water flowrate at NTP = 0.05 mL/min 150 mg catalyst	Sonochemical	320	48,000 (dry basis)	X_{CO} = 92% S_{CH4} = 0% S_{CO2} = 100%	8.36	Present Study
RuCZ (Feed B)	CO:H_2:N_2 = 2:35:63 vol% Flowrate at NTP: 100 mL/min Water flowrate at NTP = 0.05 mL/min 150 mg catalyst	Sonochemical	320	48,000 (dry basis)	X_{CO} = 96% S_{CH4} = 37% S_{CO2} = 63%	8.72	Present Study
RuCZ (Feed C)	CO:H_2:CO_2:N_2 = 2:35:14:49 vol% Flowrate at NTP: 100 mL/min Water flowrate at NTP = 0.05 mL/min 150 mg catalyst	Sonochemical	320	48,000 (dry basis)	X_{CO} = 84% S_{CH4} = 47% S_{CO2} = 53%	7.63	Present Study
PdCZ (Feed A)	CO:N_2 = 2:98 vol% Flowrate at NTP: 100 mL/min Water flowrate at NTP = 0.05 mL/min 150 mg catalyst	Sonochemical	320	48,000 (dry basis)	X_{CO} = 47% S_{CH4} = 0% S_{CO2} = 100%	4.27	Present Study
PdCZ (Feed B)	CO:H_2:N_2 = 2:35:63 vol% Flowrate at NTP: 100 mL/min Water flowrate at NTP = 0.05 mL/min 150 mg catalyst	Sonochemical	320	48,000 (dry basis)	X_{CO} = 73% S_{CH4} = 18% S_{CO2} = 82%	6.63	Present Study
PdCZ (Feed C)	CO:H_2:CO_2:N_2 = 2:35:14:49 vol% Flowrate at NTP: 100 mL/min Water flowrate at NTP = 0.05 mL/min 150 mg catalyst	Sonochemical	320	48,000 (dry basis)	X_{CO} = 56% S_{CH4} = 13% S_{CO2} = 87%	5.09	Present Study
PtCZ (Feed A)	CO:N_2 = 2:98 vol% Flowrate at NTP: 100 mL/min Water flowrate at NTP = 0.05 mL/min 150 mg catalyst	Sonochemical	300	48,000 (dry basis)	X_{CO} = 100% S_{CH4} = 0% S_{CO2} = 100%	9.09	Present Study
PtCZ (Feed B)	CO:H_2:N_2 = 2:35:63 vol% Flowrate at NTP: 100 mL/min Water flowrate at NTP = 0.05 mL/min 150 mg catalyst	Sonochemical	300	48,000 (dry basis)	X_{CO} = 96% S_{CH4} = 17% S_{CO2} = 83%	8.72	Present Study
PtCZ (Feed C)	CO:H_2:CO_2:N_2 = 2:35:14:49 vol% Flowrate at NTP: 100 mL/min Water flowrate at NTP = 0.05 mL/min 150 mg catalyst	Sonochemical	300	48,000 (dry basis)	X_{CO} = 57% S_{CH4} = 26% S_{CO2} = 74%	5.18	Present Study
KPtCZ (Feed A)	CO:N_2 = 2:98 vol% Flowrate at NTP: 100 mL/min Water flowrate at NTP = 0.05 mL/min 150 mg catalyst	Sonochemical	300	48,000 (dry basis)	X_{CO} = 100% S_{CH4} = 0% S_{CO2} = 100%	9.09	Present Study
KPtCZ (Feed B)	CO:H_2:N_2 = 2:35:63 vol% Flowrate at NTP: 100 mL/min Water flowrate at NTP = 0.05 mL/min 150 mg catalyst	Sonochemical	300	48,000 (dry basis)	X_{CO} = 98% S_{CH4} = 4% S_{CO2} = 96%	8.9	Present Study
KPtCZ (Feed C)	CO:H_2:CO_2:N_2 = 2:35:14:49 vol% Flowrate at NTP: 100 mL/min Water flowrate at NTP = 0.05 mL/min 150 mg catalyst	Sonochemical	300	48,000 (dry basis)	X_{CO} = 93% S_{CH4} = 3.3% S_{CO2} = 96.7%	8.45	Present Study

Table 2. *Cont.*

Catalyst	Feed Details	Method of Synthesis	Temperature, °C	GHSV, h^{-1}	% Conversion of CO and % CH_4, CO_2 Selectivity	Reaction Rate, $\mu mol\ g^{-1}\ s^{-1}$	Ref.
Feed A	CO:N_2 = 2:98 vol% Flowrate at NTP: 100 mL/min Water flowrate at NTP = 0.05 mL/min	No Catalyst	300	-	(with WGS alone) X_{CO} = 99.94% S_{CH4} = 0% S_{CO2} = 100% (with side reactions) X_{CO} = 99.92% S_{CH4} = 7.3% S_{CO2} = 92.7%	-	Equilibrium
Feed B	CO:H_2:N_2 = 2:35:63 vol% Flowrate at NTP: 100 mL/min Water flowrate at NTP = 0.05 mL/min	No Catalyst	300	-	(with WGS alone) X_{CO} = 98.7% S_{CH4} = 0% S_{CO2} = 100% (with side reactions) X_{CO} = 100% S_{CH4} = 100% S_{CO2} = 0%	-	Equilibrium
Feed C	CO:H_2:CO_2:N_2 = 2:35:14:49 vol% Flowrate at NTP: 100 mL/min Water flowrate at NTP = 0.05 mL/min	No Catalyst	300	-	(with WGS alone) X_{CO} = 89.3% S_{CH4} = 0% S_{CO2} = 100% (with side reactions) X_{CO} = 99.48% S_{CH4} = 49.4% S_{CO2} = 50.6%	-	Equilibrium
					(with WGS alone)		

The experimental data in the given conditions follows the Weisz–Prater correlation [50] for mass transfer limitation, indicating the validity of differential flow reactor assumption. Thus, the reaction rates were calculated by, $r_{CO} = \frac{X_{CO}}{(W/F_{CO})}$. Figure 8 shows the logarithm of rate (obtained from the slope of CO fractional conversion versus W/F_{CO}) with reciprocal of temperature, which follows the Arrhenius relationship, and the activation energies were calculated from the slopes of the linear fittings. The activation energy of KPtCZ catalyst under reformate feed condition C was found to be lowest (66 kJ mol^{-1}) compared with all other catalysts. Even under Feed B condition, the activation energy of KPtCZ was 78 kJ mol^{-1}, which was almost close to the activation energy of PtCZ. Overall, KPtCZ was found to be the best catalyst for WGS activity under reformate feed conditions. In our previous studies, the mechanistic studies of CO abatement on CO_3O_4 catalysts indicated the carbonates as key intermediates during the reaction and its dissociation to CO_2 was critical [51,52]. Under H_2 rich conditions, formate and hydroxyl species were also detected [52]. K impregnation suppresses the chemisorption affinity of electron donor species such as H_2 and allows scission of C–H bond in formate species [35,53,54]. Thus, in the present study, CO and CO_2 methanation reactions may be insignificant on the KPtCZ catalyst, leading to very low methane selectivities, as shown in Figure 7j. The lowest activation energy of KPtCZ under Feed C condition further indicates its high catalytic ability and successful resistance towards methanation. The activation energies and maximum CO conversions of the catalysts are listed in Table 3.

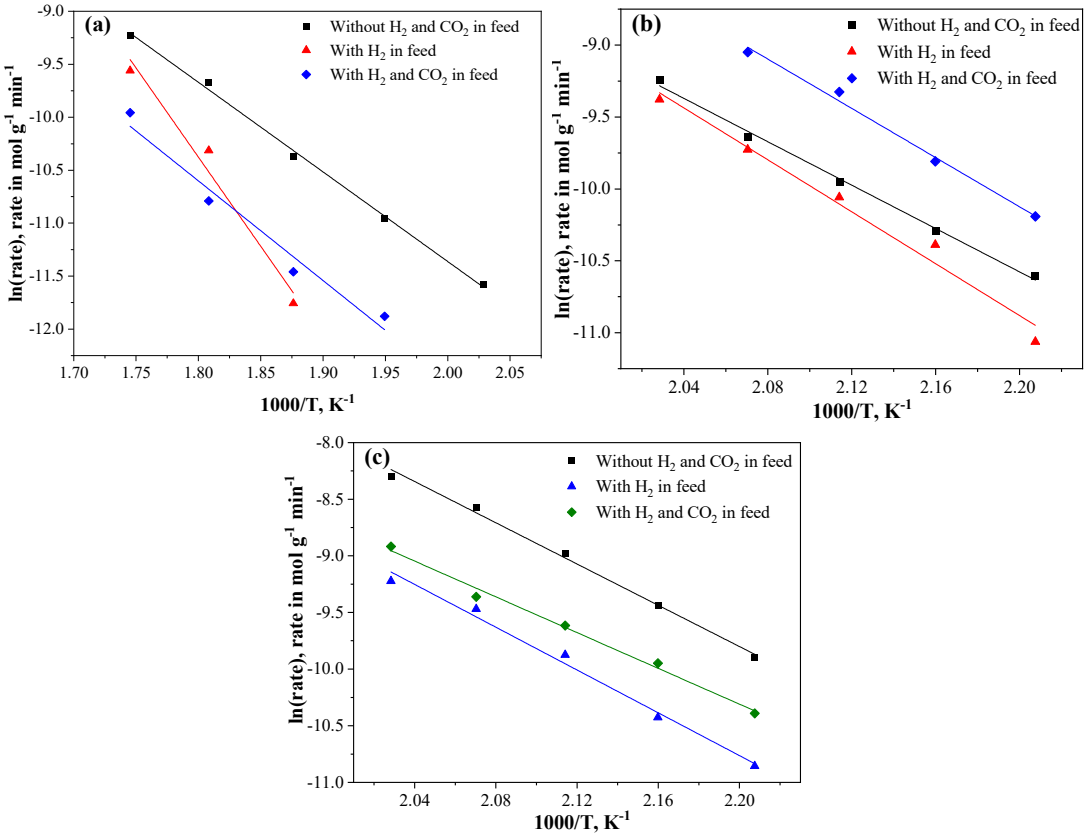

Figure 8. Arrhenius plots for (**a**) CZ, (**b**) PtCZ and (**c**) KPtCZ catalysts for WGS under different feed conditions.

Table 3. Apparent activation energy comparison with literature.

Catalyst	Maximum CO Conversion	Apparent Activation Energy, E_a kJ/mol	Temperature Range and Flow Rate, °C and mL/min	Catalyst Loading, mg	Ref.
Pt (NO)/CeO_2	~92	~73.84	250–400, 100	200	[55]
Pt/SrHAP-11	~95	70	250–450, 100	75	[56]
Cu/Pd-Ag	~95	10	200–300, 190	1500	[57]
Pt-Re (2:3)	~90	20	250, 500	120	[20]
Pd/Ceria	-	49	180	100	[58]
$Mn_{2.94}Pt_{0.06}O_{4-ö}$	100	59	180–450	100	[46]
CZ (Feed A)	~28	70 ± 5	180–300, 100	150	Present Study
CZ (Feed B)	~16	140 ± 7	180–300, 100	150	Present Study
CZ (Feed C)	~12	78 ± 4	180–300, 100	150	Present Study
PtCZ (Feed A)	~100	63 ± 2	180–300, 100	150	Present Study
PtCZ (Feed B)	~98	75 ± 3	180–300, 100	150	Present Study
PtCZ (Feed C)	~50	72 ± 3	180–300, 100	150	Present Study
KPtCZ (Feed A)	~100	75 ± 4	180–300, 100	150	Present Study
KPtCZ (Feed B)	~100	78 ± 5	180–300, 100	150	Present Study
KPtCZ (Feed C)	~90	66 ± 3	180–300, 100	150	Present Study

2.4. X-ray Photoelectron Spectroscopy Studies

Figure 9a shows Co 2p spectra of the catalyst. The presence of Co_3O_4 phase as well as the presence of negligible CoO phase was observed. The ratio of Co^{3+}/Co^{2+} was found to be 2:1. The binding energies of core level Co $2p_{3/2}$, $2p_{1/2}$ peaks were observed at 779.7 eV, 794.8 eV for Co^{3+} and 781.3 eV, 796.4 eV for Co^{2+}. The difference between Co $2p_{3/2}$ and Co $2p_{1/2}$ of Co^{3+} and Co^{2+} was 15.1 eV [59,60]. Co $2p_{3/2}$ and Co $2p_{1/2}$

shakeup peaks were observed at 783.7 and 797.9 eV, a peak corresponded to 789.4 eV in Figure 8a, which was because of the CoO satellite [61]. Figure 9b shows the Zr 3d spectra and deconvoluted according to $3d_{5/2}$ and $3d_{3/2}$ split orbitals. The peaks at 181.7 eV and 184.1 eV were assigned to $3d_{5/2}$ and $3d_{3/2}$ [62]. In KPtCZ catalyst, Pt was found in only +4 ionic states, indicating the ionic substitution (as shown in Figure 9c) and formation PtO_2 clusters. No metallic Pt was detected in KPtCZ. Deconvoluted spectra showed 74.3 eV and 77.6 eV for Pt $4f_{7/2}$ and Pt $4f_{5/2}$ core level spectra. From Figure 9, K $2p_{3/2}$ and K $2p_{1/2}$ core level peaks were observed at 292.6 eV and 295.4 eV, respectively, thus confirming the potassium presence.

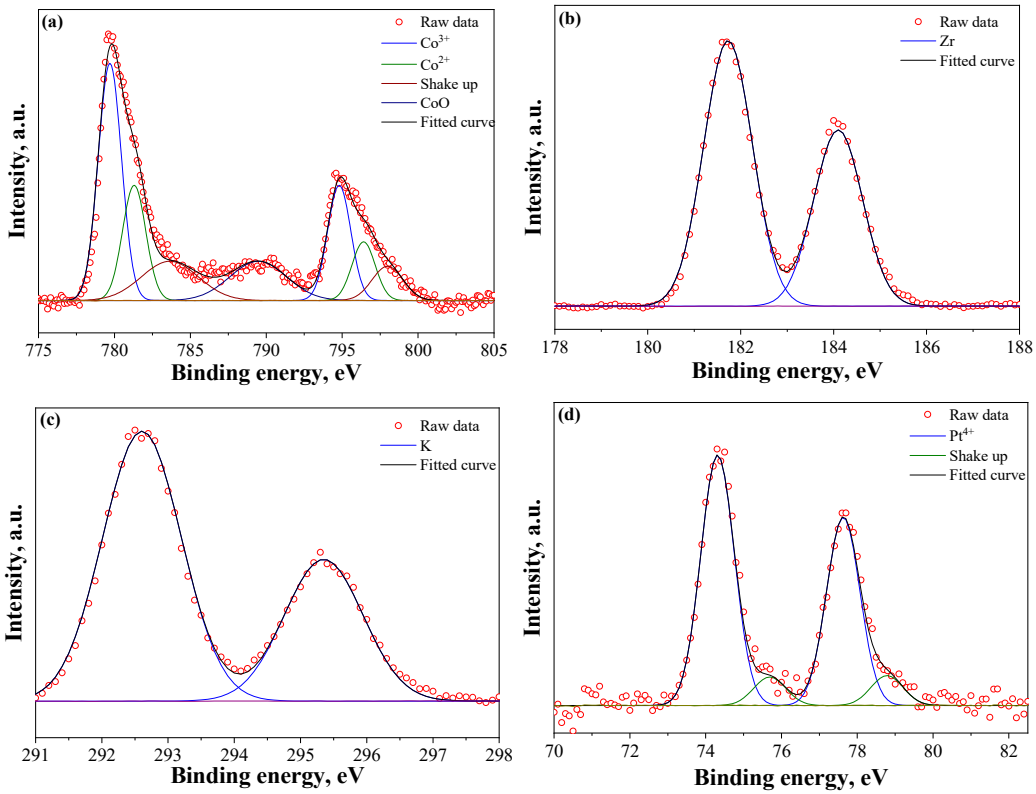

Figure 9. XPS spectra of KPtCZ catalyst (**a**) Co 2p, (**b**) Zr 3d, (**c**) K 2p and (**d**) Pt 4f core level spectra.

2.5. H_2–Temperature Programming Reduction (H_2–TPR) Analysis

As shown in Figure 10, the TPR profiles started at ~202 °C in the case of CZ, but the starting temperatures were 102 °C, 107 °C and 120 °C with PtCZ, PdCZ and RuCZ. However, the reduction peak started at 95 °C due to K deposition in the KPtCZ catalyst. RuCZ and PdCZ had a wide reduction over the temperature range of 100–900 °C [63]. This could be due to overlap with Co_3O_4 reduction peaks, which is usually limited to temperatures below 450 °C. Pd, Pt and Ru incorporation in metal oxide caused structural changes and enhanced the oxygen mobility for the reduction in supports [64,65]. The reduction peaks of Co_3O_4 also shifted to low temperatures compared with the reduction peaks in the CZ composite. The broad reduction peaks were observed at 352 °C and 358 °C for PdCZ and RuCZ. All these supports had wide reduction distribution over a temperature range up to 900 °C. However, in the case of KPtCZ similar behavior was not observed. As K impregnation itself having a chemical reduction step, the reduction peaks were noticed at 141 °C and 417 °C, which were lower temperatures than for PtCZ. This could be another reason for the good catalytic performance of KPtCZ for WGS than other catalysts, as the reduction lead to more lattice oxygen vacancies as well. Even for high temperature WGS, the operating temperatures fell below 500 °C. All synthesized catalysts showed reducible

behavior greater than 600 °C, indicating its ability towards WGS. As evident from Figure 7, KPtCZ is a potential candidate for low temperature WGS.

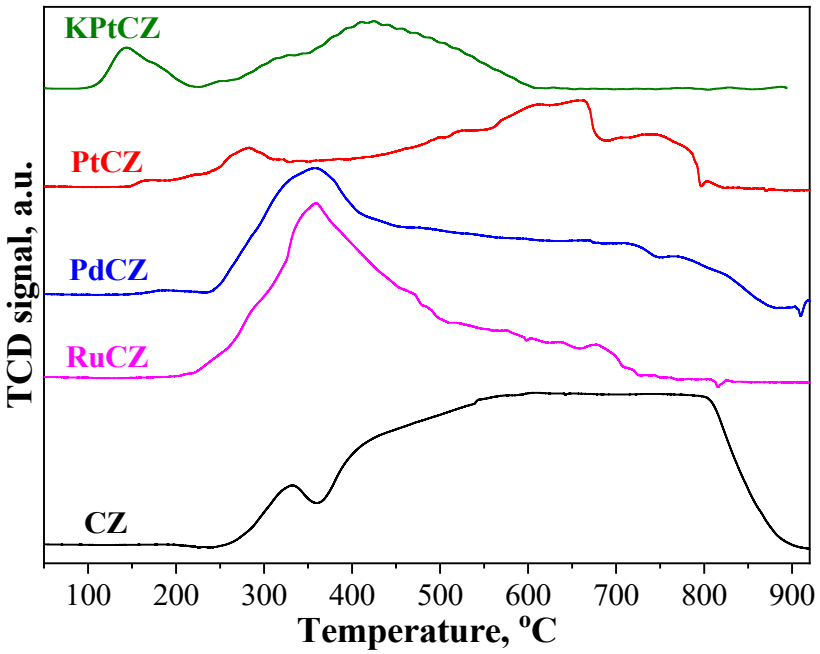

Figure 10. H_2–TPR profiles for CZ, RuCZ, PdCZ, PtCZ and KPtCZ catalysts.

3. Materials and Methods

3.1. Materials

Cobaltous nitrate hexahydrate ($Co(NO_3)_2 \cdot 6H_2O$, 98%), zirconium(IV) oxynitrate hydrate ($ZrO(NO_3)_2 \cdot xH_2O$, 99%), palladium chloride ($PdCl_2$, 99%), hexachloroplatinic acid (H_2PtCl_6, ~40%) and ruthenium chloride trihydrate ($RuCl_3 \cdot 3H_2O$, 99%) are procured from Sigma-Aldrich. Diethylene triamine (DETA), ammonia solution and polyethylene glycol powder (PEG-600) were procured from SD Fine chemicals, Maharashtra, India.

3.2. Catalyst Synthesis

M/Co_3O_4–ZrO_2 (MCZ, M = Pt, Pd and Ru) composite catalysts were synthesized by sonochemical synthesis. The synthesis protocols for PtCZ and PdCZ were adopted from our previous work [37]. A similar protocol was implemented to prepare RuCZ. In a typical synthesis, 100 mL of 1.2 mM $Co(NO_3)_2 \cdot 6H_2O$ was added dropwise to 65 mL of 1.2 mM of $ZrO(NO_3)_2 \cdot xH_2O$ under rigorous stirring. 2 g of PEG−600 was added to the solution and allowed 30 min stirring. 22 mg of $RuCl_3$ dissolved in 10 mL and added dropwise to the solution. 5 mL of diethylene triamine (DETA) was added to the solution to ensure effective doping. To this solution 0.1 M NH_4OH was added to maintain the pH of 8 under ultrasonic radiation (25 kHz, 125 W, Electrosonic Industries, Mumbai, India). The effective sonication continued for 3 h and the precipitate was separated by centrifugation. The collected precipitate was washed thrice with ethanol and dried at 120 °C for 6 h and kept for calcination at 500 °C for 2 h. The effect of K as promoter was studied for WGS activity on the best performing catalyst (PtCZ). 0.5 g of PtCZ was taken and dispersed in 500 mL of water. Under rigorous stirring, 50 mL of 5.2 mM of KOH solution was slowly added and then reduced using 2 mL of hydrazine hydrate. Further, the catalyst was allowed to mix for 12 h, the suspended nanoparticles were separated and dried on a hot plate at 120 °C for 12 h.

3.3. WGS Experimental Conditions

The catalysts were made into pellets using hydraulic press and were then crushed and a 60/80 mesh size was collected using sieves. In a typical experiment, 150 mg catalyst was

packed with ceramic glass wool plugs, at the center of 4 mm ID quartz reactor. The bed length of 1 cm was maintained by diluting the catalysts with silica. The catalyst loading varied from 50 to 200 mg. To study the effect of reformate gas mixture, different feed conditions with dry gas volume ratios of $CO:N_2$ = 2:98 (Feed A), $CO:H_2:N_2$ = 2:35:63 (Feed B) and $CO:H_2:CO_2:N_2$ = 2:35:14:49 (Feed C) were used at 1 atm. The dry gas flow rate was maintained at 100 mL/min. Then, 0.05 mL/min of water was passed using a HPLC pump through the boiler maintained at 150 °C and superheated steam to the reactor along with the dry feed. Isothermal reaction conditions were maintained at each temperature in the range of 150–400 °C and product gases were analyzed at steady state operation of 30 min. A condenser was connected at the exit of the reactor to remove the steam and the dry gases alone were allowed to pass through online gas chromatograph to analyze the outlet gas composition. The conversion of CO and selectivity of undesirable product methane were calculated using the following formulae,

$$\% \text{ CO Conversion} = \left(\frac{F_{CO,\,in} - F_{CO,\,out}}{F_{CO,\,in}} \right) \times 100 \quad (2)$$

$$\% \text{ } CH_4 \text{ Selectivity} = \left(\frac{F_{CH_4,\,out}}{F_{CH_4,\,out} + F_{CO_2,\,out}} \right) \times 100 \quad (3)$$

$$\% \text{ } CO_2 \text{ Selectivity} = \left(\frac{F_{CO_2,\,out}}{F_{CH_4,\,out} + F_{CO_2,\,out}} \right) \times 100 \quad (4)$$

Here, $F_{CO,\,in}$ and $F_{CO,\,out}$ are the molar flowrates of CO at the inlet and exit of the reactor, $F_{CH_4,\,out}$ and $F_{CO_2,\,out}$ are the exit molar flowrates of CH_4 and CO_2.

3.4. Characterization Methods

All the catalysts were characterized using XRD, XPS, TEM and BET. X-ray diffraction patterns were collected by using Rigaku X-ray diffraction equipment with 0.35°/min in the scan range of 20–80° with a Cu Kα source. XPS data were collected using AXIS ULTRA instrument with Al-Kα as radiation source and all samples were calibrated using graphic carbon at 284.8 eV. A surface area analyzer (Microtrac Bel, BELSORP Mini II, Osaka, Japan) was used to determine the surface properties of the catalysts at 77 K using liquid N_2. The scanning electron micrographs (SEM) and energy dispersive X-ray diffraction (EDX) studies for all catalysts were recorded with a high vacuum and 20 kV using an APREOS field-emission scanning electron microscope (ThermoFisher Scientific, Waltham, MA, USA). TEM micrographs for the prepared catalysts were recorded by using FEI F30 instrument (FEI Tecnai F30, Atlanta, GA, USA) operating at 200 kV.

3.5. H_2-Temperature Programmed Reduction

Temperature programmed reduction (TPR) with H_2 was performed with 10 mg of catalyst loaded in a quartz reactor. A flow rate of 30 mL/min of 5% H_2 in Ar (Chemix gases, Karnataka, India) was maintained in temperature range of 50 to 900 °C with a ramping rate of 10 °C/min using a PID controller. Hydrogen consumption during the reduction was analyzed with thermal conductivity detector connected (Mayura Analytical Private Limited, Karnataka, India) to outlet stream.

4. Conclusions

The present study focused on the water–gas shift activity of noble metal-substituted Co_3O_4–ZrO_2 (CZ) support under reformate feed conditions. To obtain maximum yield of H_2, the side reactions such as CO and CO_2 methanation must be avoided in water–gas shift stage. However, it is a challenging task to suppress the methanation under reformate feed (H_2 and CO_2 rich feed) conditions. In this study, we developed CZ, RuCZ, PdCZ, PtCZ by sonochemical synthesis. The electron donor compound, potassium, was impregnated on the surface of PtCZ supports to suppress the methanation with high CO conversions at low

temperatures. The best catalyst, PtCZ, showed high CO conversions of 100% and rate of 9.09 μmol g^{-1} s^{-1} at 300 °C. However, the conversions were observed as 96% and 57% CO conversions at 300 °C with prominent methane selectivity of 17% and 26% under Feed B and C conditions, whereas the KPtCZ catalyst showed 100% and 98% of CO conversions and rates of 9.09 and 8.9 μmol g^{-1} s^{-1} at 300 °C and no significant methane selectivity (<4%) was observed. The H_2 activation on the catalyst surface can be negligible due to K impregnation and, furthermore, it reduced the methane formation. By tuning the surface properties, stable conversions were achieved. On overall, PtCZ and KPtCZ were found to be potential candidates for low temperature water–gas shift reaction; however, KPtCZ was found to be best, with the lowest activation energy of 66 ± 3 kJ mol^{-1} under reformate feed (H_2 and CO_2 rich feed) conditions.

Author Contributions: Conceptualization, S.A.S. and G.M.; methodology, S.A.S.; validation, S.A.S., Y.V. and P.G.; formal analysis, S.A.S. and Y.V.; investigation, S.A.S. and Y.V.; resources, S.A.S., I.S. and G.M.; data curation, S.A.S. and Y.V.; writing—original draft preparation, S.A.S., Y.V. and P.G.; writing—review and editing, S.A.S. and Y.V.; supervision, S.A.S., I.S. and G.M.; project administration, S.A.S., I.S. and G.M.; funding acquisition, S.A.S. and I.S. All authors have read and agreed to the published version of the manuscript.

Funding: This research was funded by the Science and Engineering Research Board (SERB), Department of Science and Technology, India, grant number CRG/2021/000333.

Data Availability Statement: Not applicable.

Conflicts of Interest: The authors declare no conflict of interest.

References

1. Reitz, W. *Handbook of Fuel Cells: Fundamentals, Technology, and Applications*; Vielstich, W., Lamm, A., Gasteiger, H.A., Eds.; John Wiley and Sons, Ltd.: Hoboken, NJ, USA, 2007; Volume 2, pp. 5–30.
2. Reddy, G.K.; Smirniotis, P.G. Introduction about WGS reaction. In *Water Gas Shift Reaction: Research Developments and Apllications*, 2nd ed.; Reddy, G.K., Smirniotis, P.G., Eds.; Elsevier: Amsterdam, The Netherlands, 2015; pp. 1–20.
3. Tonkovich, A.Y.; Zilka, J.L.; LaMont, M.J.; Wang, Y.; Wegeng, R.S. Microchannel reactors for fuel processing applications. I. Water gas shift reactor. *Chem. Eng. Sci.* **1999**, *54*, 2947–2951. [CrossRef]
4. Potdar, H.S.; Jeong, D.-W.; Kim, K.-S.; Roh, H.-S. Synthesis of highly active nano-sized Pt/CeO_2 catalyst via a cerium hydroxy carbonate precursor for water gas shift reaction. *Catal. Lett.* **2011**, *141*, 1268–1274. [CrossRef]
5. Reddy, G.K.; Gunasekara, K.; Boolchand, P.; Smirniotis, P.G. Cr- and Ce-doped ferrite catalysts for the high temperature water−gas shift reaction: TPR and Mossbauer Spectroscopic Study. *J. Phys. Chem. C* **2011**, *115*, 920–930. [CrossRef]
6. Soria, M.A.; Pérez, P.; Carabineiro, S.A.C.; Maldonado-Hódar, F.J.; Mendes, A.; Madeira, L.M. Effect of the preparation method on the catalytic activity and stability of Au/Fe_2O_3 catalysts in the low-temperature water–gas shift reaction. *Appl. Catal. A Gen.* **2014**, *470*, 45–55. [CrossRef]
7. Bussche, K.M.V.; Froment, G.F. A steady-state kinetic model for methanol synthesis and the water gas shift reaction on a commercial $Cu/ZnO/Al_2O_3$ catalyst. *J. Catal.* **1996**, *161*, 1–10. [CrossRef]
8. Bahmani, M.; Nazari, M.; Mehreshtiagh, M. A study on the mechanical strength of $Fe_2O_3/Cr_2O_3/CuO$ catalyst for high temperature water gas shift reaction. *J. Porous Mater.* **2021**, *28*, 683–693. [CrossRef]
9. Rodriguez, J.A.; Grinter, D.C.; Liu, Z.; Palomino, R.M.; Senanayake, S.D. Ceria-based model catalysts: Fundamental studies on the importance of the metal–ceria interface in CO oxidation, the water–gas shift, CO_2 hydrogenation, and methane and alcohol reforming. *Chem. Soc. Rev.* **2017**, *46*, 1824–1841. [CrossRef]
10. Mandapaka, R.; Natarajan, P.; Madras, G. Microkinetic model for WGS over ionic platinum substituted ceria under r-WGS conditions. *Int. J. Hydrogen Energy* **2017**, *42*, 23891–23898. [CrossRef]
11. Chamnankid, B.; Föttinger, K.; Rupprechter, G.; Kongkachuichay, P. Cu/Ni-Loaded CeO_2-ZrO_2 catalyst for the water-gas shift reaction: Effects of loaded metals and CeO_2 addition. *Chem. Eng. Technol.* **2014**, *37*, 2129–2134. [CrossRef]
12. Guild, C.J.; Vovchok, D.; Kriz, D.A.; Bruix, A.; Hammer, B.; Llorca, J.; Xu, W.; El-Sawy, A.; Biswas, S.; Rodriguez, J.A.; et al. Water-Gas-Shift over metal-free nanocrystalline ceria: An experimental and theoretical study. *ChemCatChem* **2017**, *9*, 1373–1377. [CrossRef]
13. Panagiotopoulou, P.; Kondarides, D.I. Effects of alkali promotion of TiO_2 on the chemisorptive properties and water–gas shift activity of supported noble metal catalysts. *J. Catal.* **2009**, *267*, 57–66. [CrossRef]
14. Silva, L.P.C.; Terra, L.E.; Coutinho, A.C.S.L.S.; Passos, F.B. Sour water–gas shift reaction over $Pt/CeZrO_2$ catalysts. *J. Catal.* **2016**, *341*, 1–12. [CrossRef]

15. Reina, T.R.; Ivanova, S.; Delgado, J.J.; Ivanov, I.; Idakiev, V.; Tabakova, T.; Centeno, M.A.; Odriozola, J.A. Viability of Au/CeO_2–ZnO/Al_2O_3 catalysts for pure hydrogen production by the water–gas shift reaction. *ChemCatChem* **2014**, *6*, 1401–1409.
16. Aranifard, S.; Ammal, S.C.; Heyden, A. On the importance of the associative carboxyl mechanism for the water-gas shift reaction at Pt/CeO_2 interface sites. *J. Phys. Chem. C* **2014**, *118*, 6314–6323. [CrossRef]
17. Li, Y.; Fu, Q.; Flytzani-Stephanopoulos, M. Low-temperature water-gas shift reaction over Cu- and Ni-loaded cerium oxide catalysts. *Appl. Catal. B Environ.* **2000**, *27*, 179–191. [CrossRef]
18. Rodriguez, J.A.; Ma, S.; Liu, P.; Hrbek, J.; Evans, J.; Pérez, M. Activity of CeO_x and TiO_x nanoparticles grown on Au(111) in the water-gas shift reaction. *Science* **2007**, *318*, 1757–1760. [CrossRef]
19. Fu, Q.; Saltsburg, H.; Flytzani-Stephanopoulos, M. Active nonmetallic Au and Pt species on ceria-based water-gas shift catalysts. *Science* **2003**, *301*, 935–938. [CrossRef]
20. Sato, Y.; Terada, K.; Hasegawa, S.; Miyao, T.; Naito, S. Mechanistic study of water–gas-shift reaction over TiO_2 supported Pt–Re and Pd–Re catalysts. *Appl. Catal. A Gen.* **2005**, *296*, 80–89. [CrossRef]
21. Panagiotopoulou, P.; Kondarides, D.I. A comparative study of the water-gas shift activity of Pt catalysts supported on single (MO_x) and composite (MO_x/Al_2O_3, MO_x/TiO_2) metal oxide carriers. *Catal. Today* **2007**, *127*, 319–329. [CrossRef]
22. Ang, M.L.; Oemar, U.; Kathiraser, Y.; Saw, E.T.; Lew, C.H.K.; Du, Y.; Borgna, A.; Kawi, S. High-temperature water–gas shift reaction over Ni/xK/CeO_2 catalysts: Suppression of methanation via formation of bridging carbonyls. *J. Catal.* **2015**, *329*, 130–143. [CrossRef]
23. Bang, G.; Moon, D.-K.; Kang, J.-H.; Han, Y.-J.; Kim, K.-M.; Lee, C.-H. High-purity hydrogen production via a water-gas-shift reaction in a palladium-copper catalytic membrane reactor integrated with pressure swing adsorption. *Chem. Eng. J.* **2021**, *411*, 128473. [CrossRef]
24. Zhao, Z.; Wang, M.; Ma, P.; Zheng, Y.; Chen, J.; Li, H.; Zhang, X.; Zheng, K.; Kuang, Q.; Xie, Z.-X. Atomically dispersed Pt/CeO_2 catalyst with superior CO selectivity in reverse water gas shift reaction. *Appl. Catal. B Environ.* **2021**, *291*, 120101. [CrossRef]
25. Shinde, V.M.; Madras, G. Water gas shift reaction over multi-component ceria catalysts. *Appl. Catal. B Environ.* **2012**, *123–124*, 367–378. [CrossRef]
26. Shinde, V.M.; Madras, G. Synthesis of nanosized $Ce_{0.85}M_{0.1}Ru_{0.05}O_{2-\delta}$ (M=Si, Fe) solid solution exhibiting high CO oxidation and water gas shift activity. *Appl. Catal. B Environ.* **2013**, *138–139*, 51–61. [CrossRef]
27. Mandapaka, R.; Madras, G. Zinc and platinum co-doped ceria for WGS and CO oxidation. *Appl. Catal. B Environ.* **2017**, *211*, 137–147. [CrossRef]
28. Mierczynski, P.; Maniukiewicz, W.; Maniecki, T.P. Comparative studies of Pd, Ru, Ni, Cu/$ZnAl_2O_4$ catalysts for the water gas shift reaction. *Cent. Eur. J. Chem.* **2013**, *11*, 912–919.
29. Hu, J.; Guo, W.; Liu, Z.-H.; Lu, X.; Zhu, H.; Shi, F.; Yan, J.; Jiang, R. Unraveling the mechanism of the Zn-improved catalytic activity of Pd-based catalysts for water-gas shift reaction. *J. Phys. Chem. C* **2016**, *120*, 20181–20191. [CrossRef]
30. Jacobs, G.; Ricote, S.; Graham, U.M.; Davis, B.H. Low Temperature Water-Gas Shift Reaction: Interactions of Steam and CO with Ceria Treated with Different Oxidizing and Reducing Environments. *Catal. Lett.* **2015**, *145*, 533–540. [CrossRef]
31. Shinde, V.M.; Madras, G. Nanostructured Pd modified Ni/CeO_2 catalyst for water gas shift and catalytic hydrogen combustion reaction. *Appl. Catal. B Environ.* **2013**, *132*, 28–38. [CrossRef]
32. Vignatti, C.I.; Avila, M.S.; Apesteguía, C.R.; Garetto, T.F. Study of the water-gas shift reaction over Pt supported on CeO_2–ZrO_2 mixed oxides. *Catal. Today* **2011**, *171*, 297–303. [CrossRef]
33. Ding, K.; Gulec, A.; Johnson, A.M.; Schweitzer, N.M.; Stucky, G.D.; Marks, L.D.; Stair, P.C. Identification of active sites in CO oxidation and water-gas shift over supported Pt catalysts. *Science* **2015**, *350*, 189–192. [CrossRef]
34. Petallidou, K.C.; Kalamaras, C.M.; Efstathiou, A.M. The effect of La^{3+}, Ti^{4+} and Zr^{4+} dopants on the mechanism of WGS on ceria-doped supported Pt catalysts. *Catal. Today* **2014**, *228*, 183–193. [CrossRef]
35. Maneerung, T.; Hidajat, K.; Kawi, S. K-doped $LaNiO_3$ perovskite for high-temperature water-gas shift of reformate gas: Role of potassium on suppressing methanation. *Int. J. Hydrogen Energy* **2017**, *42*, 9840–9857. [CrossRef]
36. Watanabe, R.; Sakamoto, Y.; Yamamuro, K.; Tamura, S.; Kikuchi, E.; Sekine, Y. Role of alkali metal in a highly active Pd/alkali/Fe_2O_3 catalyst for water gas shift reaction. *Appl. Catal. A Gen.* **2013**, *457*, 1–11. [CrossRef]
37. Singh, S.A.; Vishwanath, K.; Madras, G. Role of hydrogen and oxygen activation over Pt and Pd-doped composites for catalytic hydrogen combustion. *ACS Appl. Mater. Interfaces* **2017**, *9*, 19380–19388. [CrossRef]
38. Xia, S.; Fang, L.; Meng, Y.; Zhang, X.; Zhang, L.; Yang, C.; Ni, Z. Water-gas shift reaction catalyzed by layered double hydroxides supported Au-Ni/Cu/Pt bimetallic alloys. *Appl. Catal. B Environ.* **2020**, *272*, 118949. [CrossRef]
39. Mamontov, E.; Egami, T.; Brezny, R.; Koranne, M.; Tyagi, S. Lattice defects and oxygen storage capacity of nanocrystalline ceria and ceria-zirconia. *J. Phys. Chem. B* **2000**, *104*, 11110–11116. [CrossRef]
40. Dvořák, F.; Farnesi Camellone, M.; Tovt, A.; Tran, N.-D.; Negreiros, F.R.; Vorokhta, M.; Skála, T.; Matolínová, I.; Mysliveček, J.; Matolín, V.; et al. Creating single-atom Pt-ceria catalysts by surface step decoration. *Nat. Commun.* **2016**, *7*, 10801. [CrossRef]
41. Shadravan, V.; Bukas, V.J.; Gunasooriya, G.T.K.K.; Waleson, J.; Drewery, M.; Karibika, J.; Jones, J.; Kennedy, E.; Adesina, A.; Nørskov, J.K.; et al. Effect of manganese on the selective catalytic hydrogenation of CO_x in the presence of light hydrocarbons over Ni/Al_2O_3: An experimental and computational study. *ACS Catal.* **2020**, *10*, 1535–1547. [CrossRef]
42. Utaka, T.; Okanishi, T.; Takeguchi, T.; Kikuchi, R.; Eguchi, K. Water gas shift reaction of reformed fuel over supported Ru catalysts. *Appl. Catal. A Gen.* **2003**, *245*, 343–351. [CrossRef]

43. Faur Ghenciu, A. Review of fuel processing catalysts for hydrogen production in PEM fuel cell systems. *Curr. Opin. Solid State Mater. Sci.* **2002**, *6*, 389–399. [CrossRef]
44. Ren, J.; Wang, Y.; Zhao, J.; Tan, S.; Petek, H. K atom promotion of O_2 chemisorption on Au(111) surface. *J. Am. Chem. Soc.* **2019**, *141*, 4438–4444. [CrossRef] [PubMed]
45. Uner, D.O.; Pruski, M.; Gerstein, B.C.; King, T.S. Hydrogen chemisorption on potassium promoted supported ruthenium catalysts. *J. Catal.* **1994**, *146*, 530–536. [CrossRef]
46. Anil, C.; Madras, G. Catalytic behaviour of $Mn_{2.94}M_{0.06}O_{4-\delta}$ (M=Pt, Ru and Pd) catalysts for low temperature water gas shift (WGS) and CO oxidation. *Int. J. Hydrogen Energy* **2020**, *45*, 10461–10474. [CrossRef]
47. Shinde, V.M.; Madras, G. Low temperature CO oxidation and water gas shift reaction over Pt/Pd substituted in Fe/TiO_2 catalysts. *Int. J. Hydrogen Energy* **2012**, *37*, 18798–18814. [CrossRef]
48. Jacobs, G.; Williams, L.; Graham, U.; Thomas, G.A.; Sparks, D.E.; Davis, B.H. Low temperature water–gas shift: In situ DRIFTS-reaction study of ceria surface area on the evolution of formates on Pt/CeO_2 fuel processing catalysts for fuel cell applications. *Appl. Catal. A Gen.* **2003**, *252*, 107–118. [CrossRef]
49. Deshpande, P.A.; Hegde, M.S.; Madras, G. Pd and Pt ions as highly active sites for the water–gas shift reaction over combustion synthesized zirconia and zirconia-modified ceria. *Appl. Catal. B Environ.* **2010**, *96*, 83–93. [CrossRef]
50. Weisz, P.B.; Prater, C.D. Interpretation of measurements in experimental catalysis. *Adv. Catal.* **1954**, *6*, 143–196.
51. Singh, S.A.; Madras, G. Detailed mechanism and kinetic study of CO oxidation on cobalt oxide surfaces. *Appl. Catal. A Gen.* **2015**, *504*, 463–475. [CrossRef]
52. Singh, S.A.; Mukherjee, S.; Madras, G. Role of CO_2 methanation into the kinetics of preferential CO oxidation on Cu/Co_3O_4. *Mol. Catal.* **2019**, *466*, 167–180. [CrossRef]
53. Ma, Y.; Liu, B.; Jing, M.; Zhang, R.; Chen, J.; Zhang, Y.; Li, J. Promoted potassium salts based Ru/AC catalysts for water gas shift reaction. *Chem. Eng. J.* **2016**, *287*, 155–161. [CrossRef]
54. Yang, X.; Su, X.; Chen, X.; Duan, H.; Liang, B.; Liu, Q.; Liu, X.; Ren, Y.; Huang, Y.; Zhang, T. Promotion effects of potassium on the activity and selectivity of Pt/zeolite catalysts for reverse water gas shift reaction. *Appl. Catal. B Environ.* **2017**, *216*, 95–105. [CrossRef]
55. Park, Y.M.; Son, M.; Park, M.-J.; Bae, J.W. Effects of Pt precursors on Pt/CeO_2 to water-gas shift (WGS) reaction activity with Langmuir-Hinshelwood model-based kinetics. *Int. J. Hydrogen Energy* **2020**, *45*, 26953–26966. [CrossRef]
56. Miao, D.; Cavusoglu, G.; Lichtenberg, H.; Yu, J.; Xu, H.; Grunwaldt, J.-D.; Goldbach, A. Water-gas shift reaction over platinum/strontium apatite catalysts. *Appl. Catal. B Environ.* **2017**, *202*, 587–596. [CrossRef]
57. Mendes, D.; Chibante, V.; Zheng, J.-M.; Tosti, S.; Borgognoni, F.; Mendes, A.; Madeira, L.M. Enhancing the production of hydrogen via water–gas shift reaction using Pd-based membrane reactors. *Int. J. Hydrogen Energy* **2010**, *35*, 12596–12608. [CrossRef]
58. Zhao, S.; Gorte, R.J. The activity of Fe–Pd alloys for the water–gas shift reaction. *Catal. Lett.* **2004**, *92*, 75–80. [CrossRef]
59. Wang, Y.; Yang, X.; Hu, L.; Li, Y.; Li, J. Theoretical study of the crystal plane effect and ion-pair active center for C–H bond activation by Co_3O_4 nanocrystals. *Chin. J. Catal.* **2014**, *35*, 462–467. [CrossRef]
60. Xie, S.; Dai, H.; Deng, J.; Liu, Y.; Yang, H.; Jiang, Y.; Tan, W.; Ao, A.; Guo, G. Au/3DOM Co_3O_4: Highly active nanocatalysts for the oxidation of carbon monoxide and toluene. *Nanoscale* **2013**, *5*, 11207–11219. [CrossRef]
61. Gwag, J.S.; Sohn, Y.K. Interfacial Natures and Controlling morphology of Co oxide nanocrystal structures by adding spectator Ni ions. *Bull. Korean Chem. Soc.* **2012**, *33*, 505–510. [CrossRef]
62. Guo, X.; Sun, T.-Q.; Cui, K. Darkening of zirconia: A problem arising from oxygen sensors in practice. *Sens. Actuators B Chem.* **1996**, *31*, 139–145.
63. Colussi, S.; Gayen, A.; Boaro, M.; Llorca, J.; Trovarelli, A. Influence of different palladium precursors on the properties of solution-combustion-synthesized palladium/ceria catalysts for methane combustion. *ChemCatChem* **2015**, *7*, 2222–2229. [CrossRef]
64. Duan, H.; Xu, D.; Li, W.; Xu, H. Study of the redox properties of noble metal/Co_3O_4 by electrical conductivity measurements. *Catal. Lett.* **2008**, *124*, 318–323. [CrossRef]
65. Luo, J.-Y.; Meng, M.; Li, X.; Li, X.-G.; Zha, Y.-Q.; Hu, T.-D.; Xie, Y.-N.; Zhang, J. Mesoporous Co_3O_4–CeO_2 and Pd/Co_3O_4–CeO_2 catalysts: Synthesis, characterization and mechanistic study of their catalytic properties for low-temperature CO oxidation. *J. Catal.* **2008**, *254*, 310–324. [CrossRef]